

CHAPTER 4

EMERGING INFRARED LASER ABSORPTION SPECTROSCOPIC TECHNIQUES FOR GAS ANALYSIS

FRANK K. TITTEL¹, RAFAL LEWICKI¹, ROBERT LASCOLA² AND SCOTT MCWHORTER²

¹Rice University, Electrical & Computer Engineering Department, Houston, TX

²Savannah River National Laboratory, Analytical Development Division, Aiken, SC

4.1 Introduction

Laser based spectroscopic techniques are useful for the quantitative detection and monitoring of molecular trace gas species in the mid-infrared spectral region because many molecules have their fundamental absorption band in this region. The spectroscopic instrumentation generates a measurable signal that depends on the absorption of the target medium. The choice of an optimum detection scheme depends on the requirements of the specific application and the characteristic features of the infrared laser source. Well established detection methods include several types of multipass gas absorption cells with the option to apply wavelength, frequency and amplitude modulation to the laser source. Internal and external cavity-enhanced spectroscopies are two methods to increase the magnitude of the molecular absorption signal. Photoacoustic and photothermal open path monitoring (with and without retro-reflector), such as light detection and ranging (LIDAR), differential optical absorption spectroscopy (DOAS), laser induced fluorescence (LIF), laser breakdown

spectroscopy (LIBS), and fiber optic or waveguide evanescent wave spectroscopy are other useful mid-infrared detection schemes. A key optical component for laser absorption spectroscopy (LAS) has been the introduction and commercial availability of high performance semiconductor lasers, in particular quantum cascade lasers (QCLs) since 1994 [1] and interband cascade lasers (ICLs) since 1995 [2, 3]. The development of both QCLs and ICLs continues worldwide [4, 5, 6, 7, 8, 9]. Quantum cascade lasers (QCLs) are useful, compact mid-infrared sources for ultra-sensitive and highly selective trace gas monitoring as the result of recent advances in their design and technology. They have been demonstrated to operate over a wide range of mid-infrared wavelengths from $\sim 3\text{--}24\ \mu\text{m}$. Pulsed and continuous wave (CW) QCL devices capable of thermo-electrically cooled, room-temperature operation are commercially available in the $\sim 4\text{--}12\ \mu\text{m}$ spectral region [5, 10]. These devices have several important practical features, including single mode emission with mode-hop free frequency tuning, high power (tens to hundreds of mWs) and intrinsic narrow emission line widths. These spectral characteristics permit the development of robust and fieldable trace gas sensors [11, 12, 13, 14]. For example, the Rice Laser Science Group has explored the use of several methods for carrying out infrared laser absorption spectroscopy (LAS) with mid-infrared QCL, ICL and laser diode (LD) sources, which include LAS based on multipass gas cell [15], cavity ring down spectroscopy (CRDS) [16], integrated cavity output spectroscopy (ICOS) [17, 18], photoacoustic spectroscopy (PAS) and quartz-enhanced photoacoustic spectroscopy (QEPAS) [19, 20, 21, 22, 23]. These spectroscopic techniques permit the detection and quantification of molecular trace gases with demonstrated detection sensitivities ranging from parts per million by volume (ppmv) to parts per trillion by volume (pptv) levels depending on the specific gas species and the detection method employed.

4.2 Laser Absorption Spectroscopic Techniques

In conventional absorption spectroscopy (CAS), using broadband incoherent radiation sources, such as thermal emitters, the wavelength resolution is determined by the resolving power of the spectral analyzer or spectrometer. LAS, on the other hand, uses coherent light sources, whose linewidths can be ultra-narrow and whose spectral densities can be made many orders of magnitude larger ($\sim 10^9\ \text{W}/\text{cm}^2\ \text{MHz}$) than those of incoherent light sources. The key advantages of mid-infrared LAS include:

1. An absorption spectrum that can be acquired directly by scanning the laser source across a desired rotational-vibrational resolved feature of the target analyte;
2. High detection sensitivity with maximum accuracy and precision;
3. Improved spectral selectivity, when compared to CAS due to the narrow linewidths of CW QCLs (i.e., $\sim 0.1\text{--}3\ \text{MHz}$ with a high quality power supply or $< 10\ \text{kHz}$ with frequency stabilization and for pulsed QCLs of $\sim 300\ \text{MHz}$) [24];
4. Fast response time (< 1 second in some applications);

5. Good spatial resolution, e.g., mm scale imaging of plasmas [25];
6. Detector noise that becomes negligible for sufficiently large laser intensities;
7. Non-intrusive methods to suppress laser intensity fluctuations, such as balanced detection or zero air subtraction, that can be readily applied to increase the signal-to-noise ratio (SNR) and hence improve detection sensitivity;
8. Spatially coherent laser light that can be collimated, which allows the use of long pathlength gas absorption and CRDS cells;
9. The ability to lock the laser frequency to the center of a resolved molecular absorption line, in order to determine the concentration levels of the target analyte with ultra high precision and accuracy;
10. Size, weight, electrical power, thermal management, gas and wavelength calibration, protection from harsh environment, autonomous operation and remote access for long periods of time and;
11. Ease of instrument operation and data acquisition and analysis.

During the past 25 years, mid-infrared LAS techniques have become widely commercially available. The primary uses to date have been in the spectral region $\sim 3\text{--}12\text{ }\mu\text{m}$, which covers a substantial portion of the spectrum of fundamental molecular vibrations. Wider spectral coverage from $2\text{--}24\text{ }\mu\text{m}$ has been demonstrated and reported in the literature using Sb based LDs, ICLs, and QCLs [5, 10, 26, 27]. Expansion into the vibrational overtone region ($3\text{--}5\text{ }\mu\text{m}$) is also possible with optical parametric oscillators (OPOs) and sources based on difference frequency generation (DFG). Mid-infrared absorption spectra of several small molecules of potential interest for trace gas monitoring are shown in Figure 4.1. In this figure, which highlights environmental applications, certain spectral regions are shown to be unavailable due to absorption by water and carbon dioxide. For other applications, such as specialty and electronic gas purity measurements, it will be other bulk gases which block different parts of the spectrum. Regardless, there is usually a transmission window where analyte absorption lines can be cleanly accessed. In some cases, these may be less intense overtone or combination lines rather than intense fundamental absorption lines. High sensitivity (ppmv to pptv) measurements have been demonstrated using all types of lines in both laboratory and field applications.

The primary requirements for trace gas sensing are sensitivity, selectivity and response time. For small molecules with resolved rotational structure, the selectivity is obtained by choosing an absorption line that is free of interference from other species that might be present in the analyzed sample and by implementing a laser source that possesses a sufficiently narrow linewidth. For small molecules, selectivity is further enhanced by reducing the sample pressure to sharpen the absorption line without reducing the peak absorption. This condition continues until the linewidth begins to approach the Doppler width [28].

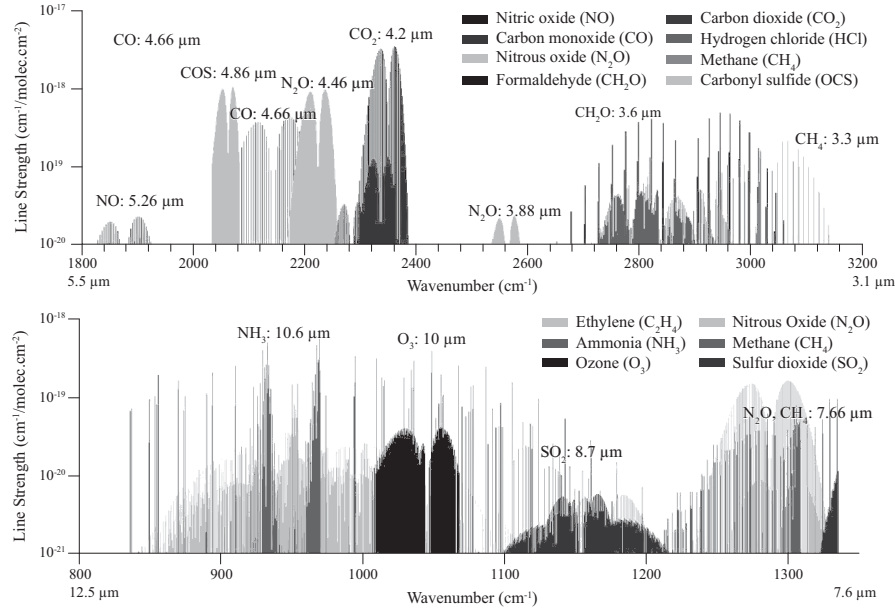


Figure 4.1 High resolution transmission molecular absorption database simulation of absorption spectra in two mid-infrared atmospheric transmission windows. With kind permission from Springer Science+Business Media: [21], fig. 1.

The fundamental behavior of laser absorption spectroscopy at a certain frequency ν [cm^{-1}] can be expressed by Beer–Lambert’s law:

$$I(\nu) = I_0(\nu)e^{-\alpha(\nu)L} \quad (4.1)$$

where $I(\nu)$, $I_0(\nu)$ are the intensities of the transmitted and incident laser light, respectively, $\alpha(\nu)$ is the absorption coefficient [cm^{-1}], and L is the effective optical pathlength [cm]. Therefore, to obtain the optimum absorption sensitivity it is necessary to choose a strong molecular absorption line, use a platform with a long effective optical pathlength, and have a distinguishable absorption from baseline variations and laser power fluctuations. The first requirement is best met by choosing a target line associated with fundamental absorption bands, as these are stronger than overtone or combination bands. A sufficiently long pathlength can be obtained by using multipass gas cells or cavity enhancement techniques. For sharp absorption lines, noise associated with laser power fluctuations can be reduced by averaging rapid scans over the time or by employing a modulation spectroscopy technique in the kHz regime [29, 30]. In most applications, one detects the modulated absorption at twice the modulation frequency using a lock-in amplifier set to $2f$. The second harmonic signal is maximized at the absorption line center. The final requirement to distinguish absorption from baseline variations is the most challenging. Every long pass arrangement exhibits accidental étalons, which typically have widths compara-

ble to that of an absorption line. In principle, these can be removed by evacuating the cell, replacing the sample with “zero air” gas, which contains no trace gas species of interest, and then dividing the sample trace by this background trace. However, this approach assumes, often incorrectly, that these accidental étalons do not shift their pattern during the process of sample replacement [10]. Numerous research groups [31, 32, 33, 34, 35] have investigated and reported on the merits of rapid background subtraction, in particular wavelength modulation spectroscopy (WMS) and frequency modulation spectroscopy (FMS) to effectively remove optical noise.

For more complex, multi-atomic molecules, which do not have resolved rotational structure, the spectroscopic detection process is more demanding. A convenient method to distinguish sample and background absorptions is by pumping the sample out and replacing it with zero air due to the absence of a nearby baseline for comparison. For weak absorption features, this imposes severe limits on the long term power stability of the laser source, the absence of low frequency laser noise, and baseline stability. Furthermore, in the mid-infrared fingerprint region, where many gases absorb, there may be other gases contributing to a broad absorption that will significantly decrease the selectivity of concentration measurements.

For open path systems, difficulties for selective measurements will be encountered because 1) there is no way to replace the sample with zero air for providing a baseline trace, and 2) there is no way to reduce the linewidths (typically 0.1 cm^{-1} at atmospheric pressure) which in some cases might be too large to perform wavelength modulation spectroscopy at an optimum modulation depth. LAS based on a multipass cell suffers from neither of these problems. The only issue with this approach is that long path multipass cells are intrinsically bulky. Long optical pathlengths are obtained by employing multipass absorption cells where the optical beam is reflected back and forth between highly reflective spherical or cylindrical mirrors. Numerous implementations have been reported in the literature, but four fundamental designs (White, Herriott, astigmatic Herriott, and Chernin) have been used to achieve optical pathlengths of $\sim 100\text{ m}$ for $\sim 0.5\text{ m}$ distance between the mirrors [36]. Furthermore, cavity enhanced spectroscopy can increase the detection sensitivity even more. CRDS has been demonstrated to offer excellent trace gas detection sensitivity [16, 37, 38], using high quality, low loss mirrors. Long pathlengths in small volumes can be achieved by off-axis ICOS, which has demonstrated considerable promise for trace gas sensing [17, 18, 39]. Other ultra sensitive and highly selective spectroscopic techniques for trace gas detection that have been reported by various research groups are: balanced detection [40], laser induced breakdown spectroscopy (LIBS) [41], noise immune cavity enhanced optical heterodyne molecular spectroscopy (NICE-OHMS) [42, 43], Faraday rotation spectroscopy [44, 45, 46], conventional photoacoustic spectroscopy (CPAS) [47, 48], QEPAS [49, 50], and direct frequency-comb spectroscopy (DFCS) [51, 52, 53, 54, 55]. The latter three techniques in addition to CRDS and ICOS will be described later in this chapter.

4.2.1 Quantum and Interband Cascade Lasers

The expansion of LAS into a routinely deployable field portable analytical instrument is primarily attributed to the development of QCL and ICL technology. Both QCLs and ICLs are smaller, easier to operate, and more rugged than other mid-infrared laser technologies, such as nonlinear optical techniques (OPO and DFG based instrumentation), and lead-salt diodes that require cryogenic cooling. As cascade lasers are becoming the dominant technology for IR LAS, a brief description of their properties and use is described. More detailed descriptions can be found in recent review articles [5, 10] and in vendor literature.

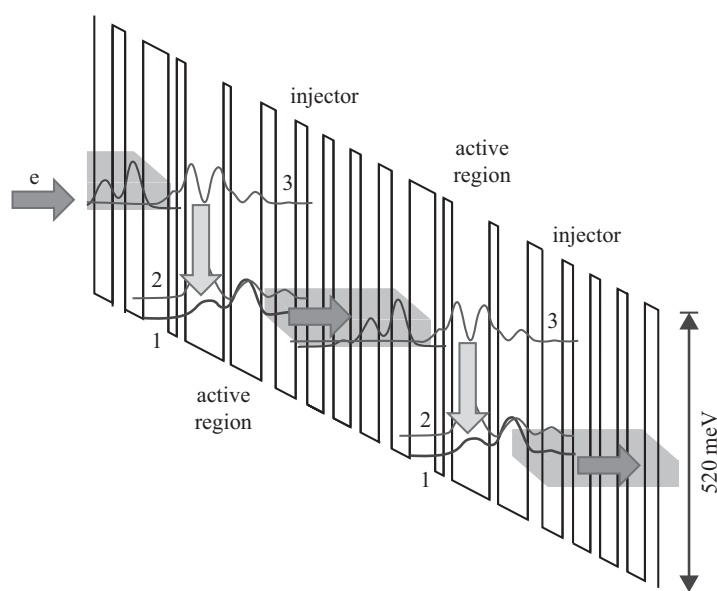


Figure 4.2 Schematic diagram indicating the quantum well based energy levels that forms the basis of QCLs. An electron injected into state three in the active region emits a photon when relaxing to state two. After relaxing to state one (through emission of a phonon), the electron is coupled into a miniband of states in the injector, and eventually into the upper level of the next active region. The period of this structure is $\sim 50\text{--}60$ nm. Reprinted from [10] with permission from Elsevier.

The unique property of QCLs compared to conventional diode lasers is the nature of the energy levels in which a population inversion is created. In diode lasers, the active region is a semiconductor with a bandgap matching the desired output wavelengths. Electron-hole pairs are injected into the active region and emit light upon electron relaxation from the conduction to valence bands.

Energy levels in a QCL arise from a quantum mechanical effect, as illustrated in a simplified manner in Figure 4.2. The laser material consists of a repeating pattern of stacks of sub-micron layers of semiconductors. The pattern includes an active region and an injector region. Electrons in the active region will experience a few

discrete energy levels. Light emission occurs when the electrons relax from upper to lower energy levels (state three to state two) within a conductive band. To maintain the population inversion, the population in state two must be drained more rapidly than the lifetime associated with the three–two transition. This is accomplished by relaxation through resonant scattering of a phonon to state one. Migration of the electron in state one to the next injector region is accomplished by providing a high density (“miniband”) of states in the injector region and applying a potential across the stack that allows those states to be in resonance with state one. The electron relaxes to the ground state of the miniband, which is in resonance with the excited energy level of the next active region. The potential also defines the energy separation of the miniband ground state and state two in the active region, suppressing thermal re-population of state two. In this manner, a single electron can be propagated through multiple active regions, emitting a photon in each one, leading to the “cascade” effect. Practical cascade laser designs have additional energy levels in the active region to help maintain population inversion and to create a broader gain spectrum, but follow this general scheme.

Emitted light is captured in a waveguide which is directly coupled to the semiconductor stack. The waveguide is narrow, increasing the coupling efficiency, but resulting in a highly divergent beam that requires high numerical aperture optics for collection and collimation. Mid-infrared semiconductor lasers can be chosen to operate in either pulsed or continuous wave (CW) mode. CW mode provides a narrower spectral linewidth (e.g., as low as 0.001 cm^{-1}) and reduced susceptibility to nonlinear optical effects, which can bias quantitative measurements if not carefully considered [10]. Laser powers of up to several hundred milliwatts are commercially available. Pulsed laser devices have fewer issues with heat management, and can be operated at room temperature, whereas CW lasers may require additional chilled water and/or air cooling. Pulses are typically of nanosecond duration, and such QCLs can be operated at Hz–kHz repetition rates. QCLs, ICLs and LDs are available in the spectral range from 3–12 μm . The spectral range of an individual mid-infrared laser is determined by its mode of operation.

The optimum operating mode for a QCL, ICL or LD for LAS is one that generates single frequency radiation. This operating characteristic can be obtained by means of distributed feedback (DFB) structure, in which the lasing wavelength is selected by a grating that is etched directly onto the laser cavity. Spectral tuning is achieved through current or laser temperature changes, which alters the refractive index of the laser waveguide material and changes the Bragg scattering condition for the grating. The scanning range for DFB–QCLs is narrow, typically 5–10 cm^{-1} . Thus, detection, quantification and monitoring of multiple analytes with a single laser is dependent on a fortuitous overlap of absorption features. One recent approach to expand the spectral range is to fabricate multiple QCLs on a single chip, exciting each one individually and adjusting chip temperature as required for accessing the desired wavelength/wavenumber. A spectral tuning range of $\sim 85\text{ cm}^{-1}$ has been demonstrated [57].

Alternatively, a wider spectral coverage can be achieved by broadening the bandwidth of the active region and utilizing an external cavity (EC) to promote lasing at

a particular wavelength [58]. The most effective means of expanding the bandwidth is to design the stack so that one or both levels in the lasing transition are replaced by a continuum of states. Additionally, a heterogeneous structure can be engineered so that a chip contains multiple energy well depths. Combining these approaches has resulted in gain bandwidths of 500 cm^{-1} . Wavelength tunability is achieved by angle control of an external grating placed in a Littrow configuration. Mode hopping of the QCL cavity and the external cavity is avoided by careful tuning of the cavity lengths with piezoelectric or temperature control [10]. These factors limit the amount of the full bandwidth that can be accessed in one device; however, a mode hop-free tuning range of 60 cm^{-1} is typical, and linewidths are comparable to those observed for DFB-QCLs.

4.2.2 Cavity Enhanced Spectroscopy: CRDS and ICOS

The conventional method to perform sensitive laser based absorption spectroscopy measurements is to increase optical pathlength by using an optical multipass gas cell. However, such an approach can be difficult to implement in field applications requiring a compact gas sensor system. For example, a typical commercial 100 m effective pathlength multipass gas cell has a volume of 3.5 L [10]. An alternative spectroscopic technique to obtain a long optical path is to make the light bounce along the same path between two ultra low-loss dielectric mirrors forming a high finesse optical resonator, that behaves as a ring-down cavity (RDC). Cavity ring-down spectroscopy is based on the principle of measuring the rate of decay of light intensity inside the RDC. The transmitted wave from an injected pulsed or CW laser into the RDC decays exponentially in time. The decay rate is proportional to the losses inside the RDC. For typical RDC mirrors having a reflectivity of 99.995%, and spaced $\sim 20\text{ cm}$, an effective optical pathlength of 8 km is obtained. This exceeds the best performance of multi-pass cell spectroscopy and uses a smaller cell volume ($\sim 25\text{ cm}^3$, depending on window/cell diameter and length). The light leaking out of the RDC can be used to characterize the absorption of the intracavity medium. The optical loss is the difference between total cavity losses and empty cavity losses. Once the absorption spectrum of the sample has been measured, then the concentration of the target analyte can be determined using the absorption cross-section and the lineshape parameters. A well designed CRDS system can achieve a minimum detectable absorption limit of $\sim 4 \times 10^{-10}$. Detailed mathematical treatment of CRDS is described in the literature [59, 60].

Several platforms exist to perform CRDS [61, 62, 63] or ICOS and its variant, off-axis ICOS (OA-ICOS), a technique where one observes time integrated ring-down events [18, 39, 64, 65]. In these techniques the coupling efficiency of the laser radiation into the resonant cavity is critical and determines the amount of light which can be collected by a photodetector placed after the absorption cell. The CRDS technique is intrinsically background-free and requires only high quality cavity mirrors, a fast detector and appropriate data acquisition electronics. A conventional CRDS based sensor platform is shown schematically in Figure 4.3. During a typical implementation, the CW laser is scanned slowly by dithering the CRD cavity length

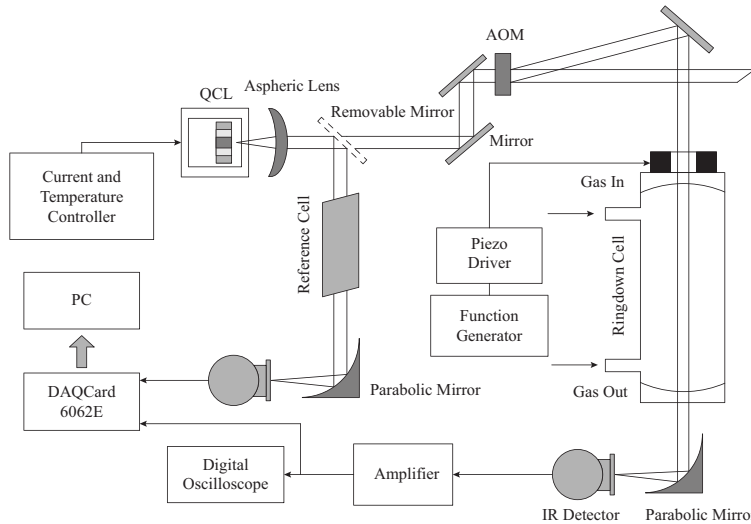


Figure 4.3 A typical CRDS based sensor platform using an acousto-optic modulator as a high speed beam chopper.

using a piezo microactuator [16, 37, 67, 66]. Commercial systems are available from several suppliers such as Los Gatos Research, Inc., Tiger Optics and Neoplas. For OA–ICOS in which the optical sensor system is aligned in such a way that a maximum number of longitudinal and transverse modes is excited within the cavity, the typical optical throughput of the cavity is on the order of $\leq T/2$ (where T is transmission of the cavity mirrors) [68]. This method is related to absorption spectroscopy using a multipass cell; however in ICOS, the beams are allowed to overlap on the mirrors after many cavity passes. The principal effect limiting sensitivity is output fluctuations caused by transmission noise due to the resonant mode structure. One approach for minimizing this noise is to arrange the laser spots on the mirrors in a circular pattern similar to those of a Herriott multi-pass cell. If many passes of the cavity occur before any of these spots overlap, interference effects are minimal because the pathlength before overlap exceeds the coherence length of the laser. By introducing a small amount of astigmatism, the entire surface of the mirrors can be used [68]. Another approach for removing mode noise in OA–ICOS is to vibrate the mirrors [17, 69]. This approach causes many mode hops to take place within the time required for light to travel its optical path in the cavity, effectively averaging out transmission noise. Thus the trade-off between multi-pass absorption and ICOS is that in multi-pass absorption, this mode noise is not present because the spots never overlap, but for similar mirror size and separation, the total pathlength can be much greater in ICOS. Since there are no mirror holes in the ICOS cavity configuration to admit and allow the exit of the beam (laser radiation is transmitted through the cavity mirrors), ICOS requires more laser power, which is now readily available with QCL

excitation. QCL-based ICOS has been used to detect hydrogen cyanide (HCN) in an argon-methane-nitrogen microwave plasma [25], in addition to monitoring acetylene impurities in ethylene manufacturing [56]. More recently, an OA–ICOS instrument for the measurement of isotope ratios in water in order to obtain information about the role of water in global climate change was reported [70]. Furthermore, by combining OA–ICOS with multiple line integrated absorption spectroscopy a sensitivity of 28 ppt for nitrogen dioxide detection in air was reported [71].

4.2.3 Conventional and Quartz Enhanced Photoacoustic Spectroscopy

Conventional photoacoustic spectroscopy (CPAS) is a well-established trace gas detection method based on the photoacoustic effect. In this method the acoustic wave is created as a result of molecular absorption of laser radiation which is either wavelength or intensity modulated. Such an acoustic wave, when it propagates within the photoacoustic (PA) cell, can be detected by a sensitive microphone [72, 73]. Instead of a single microphone device, an array of microphones is employed in some CPAS systems to achieve more sensitive results for trace gas detection [74, 75]. In contrast to other infrared absorption techniques, CPAS is an indirect technique in which the effect on the absorbing medium, rather than the direct light attenuation, is analyzed. Therefore, no photodetector is required for the CPAS technique. A low cost infrared detector located after the photoacoustic cell is usually employed for the purpose of monitoring laser power and performing a line locking procedure of the laser frequency to the wavelength of the peak of the selected absorption.

In order to obtain an optimal acoustic signal for amplitude modulated CPAS measurements, the laser modulation frequency is selected to match the first longitudinal acoustic resonance of the PA cell, given by the equation

$$f = \frac{\nu}{2L} \quad (4.2)$$

where ν is the speed of sound and L is the photoacoustic cell length. The resonance frequencies of PA cells are usually designed to be > 1 kHz, in order to make the CPAS technique immune to intrinsic $1/f$ type noise of the microphone and its pre-amplifier as well as to low frequency external acoustic noise [48, 76, 77].

The detected photoacoustic signal (S_{PA}) is described by the following equation:

$$S_{PA} = CP\alpha cM \quad (4.3)$$

where C is the photoacoustic cell constant [$\text{Pa}/(\text{W cm}^{-1})$], P is the optical power of the excitation laser [W], α is the absorption coefficient of the targeted gas [$\text{cm}^{-1}/(\text{molecule cm}^{-3})$], c is the analyte concentration [$\text{molecule}/\text{cm}^{-3}$], and M is the microphone responsivity [V/Pa].

Ideally, CPAS is a background-free technique because only the absorption of modulated laser radiation generates an acoustic signal. However, background signals can originate from nonselective absorption of the gas cell windows (coherent noise) and external acoustic (incoherent) noise. Therefore, proper isolation of the photoacoustic

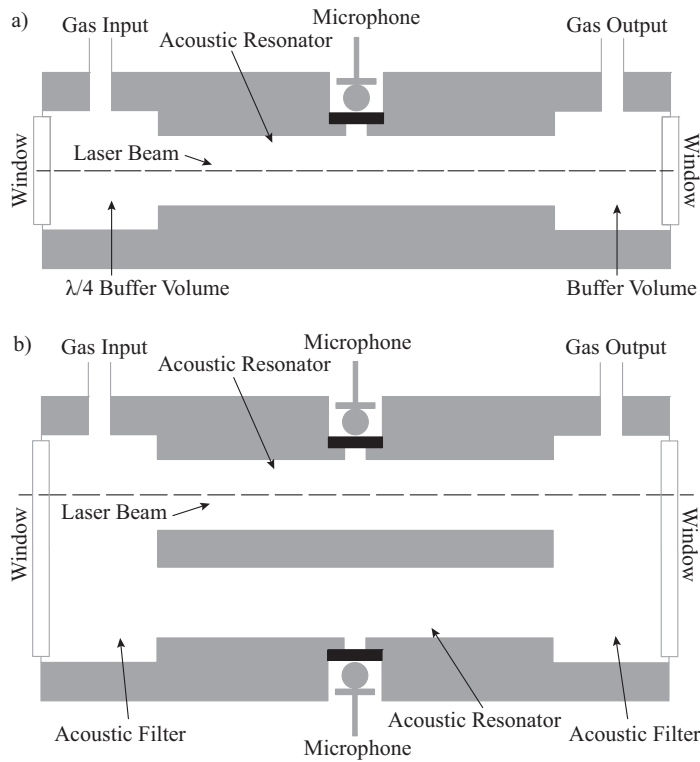


Figure 4.4 a) Block diagram of a two buffer tubes PA cell design; and b) A ring differential resonance photoacoustic cell design.

cell from any mechanical vibrations will result in an improvement of the measured SNR. Further CPAS signal enhancement can be achieved by employing a different PAS cell design, such as a resonance photoacoustic cell with two buffer tubes [78] or a ring differential resonance photoacoustic cell [79, 80]. Schematic diagrams of both designs are depicted in Figure 4.4. In the two buffer tubes photoacoustic cell design (Figure 4.4a), the $\lambda/4$ buffer volume in line with the longitudinal acoustic resonator acts as an acoustic notch filter at the frequency of the resonator, in order to effectively suppress system flow noise [81]. In a differential photoacoustic cell (Figure 4.4b), two identical cylindrical channels are equipped with a microphone, which is placed in the middle of each channel, where the maximum pressure oscillations are observed. Because CPAS signal is proportional to the absorption coefficient and the laser power, it is possible for both designs to achieve minimum detectable concentrations at the sub-ppbv level by selecting the strongest absorption lines of the target gas and by using high power laser sources such as fiber amplifiers, CW DFB-QCLs or EC-QCLs [82, 83, 84, 85, 86, 87, 88, 89].

A novel approach to photoacoustic detection of trace gases utilizing a quartz tuning fork (QTF) as an acoustic transducer, was first reported in 2002 [90, 50]. The key innovation of this new method, named quartz enhanced photoacoustic spectroscopy (QEPAS), is to invert the common CPAS approach and accumulate the acoustic energy in a sharply resonant piezoelectric transducer with a very high quality factor (Q-factor) of 10,000, rather than in a broadband microphone and low Q (~ 200) resonant CPAS gas cell. A suitable candidate for such a transducer is a QTF, which is commonly used as a frequency standard in digital clocks and watches. When the QTF is mechanically deformed, electrical charges are generated on its surface only when the two prongs move in opposite directions (antisymmetric mode of vibration). Thin silver films deposited on the quartz surfaces collect these charges, which can then be measured as either a voltage or a current, depending on the electronic circuit used. QTFs typically resonate at 32,768 (2^{15}) Hz, which results in a high immunity of QEPAS devices to environmental acoustic noise.

The photoacoustic signal measured by a QEPAS sensor is proportional to:

$$S_0 \sim \frac{\alpha \cdot P \cdot Q}{f_0} \quad (4.4)$$

where α is an absorption coefficient, P is the optical power, Q is the quality factor and f_0 is the resonant frequency [20]. The Q-factor depends upon pressure p and can be expressed as:

$$Q = \frac{Q_{vac}}{1 + Q_{vac} \cdot a \cdot p^b} \quad (4.5)$$

where Q_{vac} is the quality factor in vacuum and a and b are parameters dependent on a specific QTF design [50]. The pressure corresponding to the optimum sensitivity depends upon the vibrational to translational (V-T relaxation) energy transfer cross-section of the gas of interest. In addition, if the V-T relaxation rate is lower than the optical excitation modulation frequency, the amplitude of the optically induced acoustic signal is reduced. This effect is more significant for QEPAS due to the high modulation frequency that is used. It is more likely to occur with small (2–3 atoms) molecules such as nitric oxide, carbon monoxide, or carbon dioxide, which do not have a dense ladder of energy levels to facilitate fast V-T relaxation. The optimum pressure for fast-relaxing molecules with resolved optical transitions is < 100 Torr, which also ensures Doppler-limited spectral resolution [50]. For slow relaxing gases, this optimum pressure is higher and will lead to a broader linewidth than is desirable for the best detection selectivity.

In a typical QEPAS scheme the laser beam is focused between the QTF prongs as shown in Figure 4.5a. In this case, the probed optical path is only as long as thickness of the QTF, or ~ 0.3 mm. Therefore, QEPAS is mostly sensitive to a sound source positioned in a 0.3 mm gap between the prongs. Sound waves from distant acoustic sources tend to move the QTF prongs in the same direction, which results in a zero net piezo-current and makes this element insensitive to such external excitation. The configuration depicted in Figure 4.5a can be useful when the excitation radiation cannot be shaped into a near-Gaussian beam, as for example, with spatially multimode

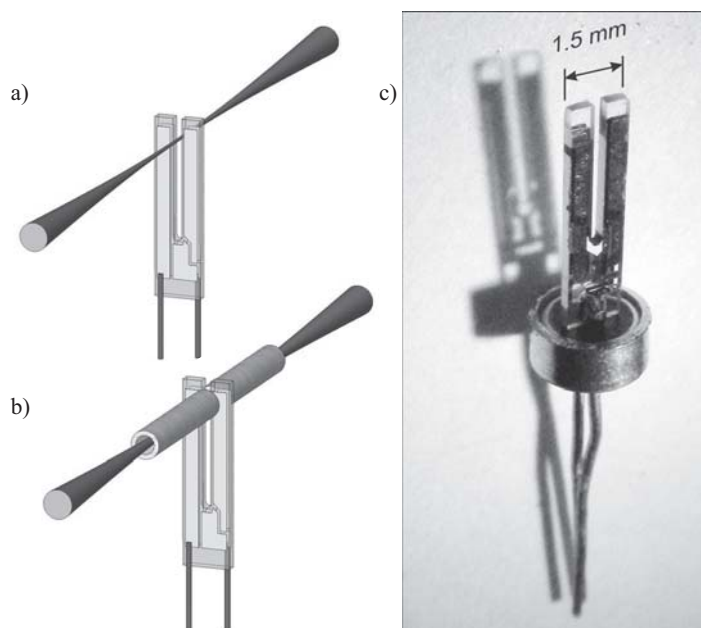


Figure 4.5 QTF based spectrophones: a) simplest spectrophone configuration and b) an improved spectrophone configuration with an acoustic resonator formed by two tubes, and c) a typical quartz tuning fork geometry used in QEPAS trace gas measurements. Figure 4.5 a) and b) with kind permission from Springer Science+Business Media: [22], fig. 1.

lasers. The simplest QEPAS configuration with bare QTF was used in preliminary evaluation tests [91] and theoretically analyzed [92]. However, the trace gas detection sensitivity can be significantly improved using the configuration shown in Figure 4.5b, where a metal tube is added on each side of QTF to confine the optically generated acoustic vibrations in the gas and increase the effective interaction length between the radiation-induced sound and the QTF [93]. The two tubes act as an acoustic microresonator with respect to the QTF resonator. Recent experimental studies have shown that the optimum length for each microresonator tube is between $\lambda_s/4$ and $\lambda_s/2$ of the propagating sound wavelength (λ_s) [19]. Thus, for an optimal microresonator (mR) configuration, where each mR tube is 4.4 mm in length and a 0.6 mm inner diameter, an improvement in the SNR of up to 30 times is obtained in comparison to the bare QTF configuration [19]. Most QEPAS based sensors utilize a configuration illustrated in Figure 4.5b. A typical quartz tuning fork, used in most QEPAS measurements to date, is illustrated in Figure 4.5c. Other QEPAS spectrophone configurations, such as off-beam QEPAS, are also possible [94, 95]. Furthermore, two novel modifications of the QEPAS sensor architecture based on interferometric photoacoustic spectroscopy [96] and resonant optothermoacoustic detection [97] were reported recently.

As in CPAS, QEPAS does not require optical detectors and also benefits from high optical output powers from commercial mid-infrared laser source. This feature is especially attractive for trace gas sensing in the 3–13 μm spectral region, where the availability of high performance optical detectors is limited. In spectroscopic measurements based on the QEPAS technique, either the laser wavelength is modulated at $f_m = f_0/2$, or its intensity is modulated at $f_m = f_0$ frequency (where f_0 is the QTF resonant frequency), depending on whether wavelength modulation or amplitude modulation technique is used. In most QEPAS sensor designs, a $2f$ wavelength modulation spectroscopy has been used [20, 21, 28, 49, 91, 93, 98, 99, 100, 101]. This technique provides complete suppression of coherent acoustic background that might be created when stray modulated radiation is absorbed by nonselective absorbers, such as the gas cell elements and the QTF itself. In this case, the noise floor is usually determined by thermal noise of the QTF [102]. In case of an amplitude modulation (AM) mode, the QEPAS sensitivity limit is no longer determined by the QTF thermal noise alone, but by laser power fluctuations and spurious interference features as well. Therefore, the AM mode is often used for detecting large, complex molecules, when individual ro-vibrational transitions are not resolved and applying wavelength modulation technique is not possible [23, 103, 104, 105, 106].

A direct, side-by-side comparison of a QEPAS sensor using a microresonator-QTF spectrophone and a CPAS sensor based on a state-of-the-art differential resonance PA cell was demonstrated by Dong, et al. in 2010 [19]. Using a $2f$ wavelength modulation technique, the detection sensitivity obtained for both QEPAS and CPAS were within the same detection range for both fast (10 ppmv acetylene in nitrogen) and slow (pure carbon dioxide) relaxing molecules. A small practical advantage of the CPAS technique over the QEPAS technique for the analysis of pure carbon dioxide results from a lower modulation frequency and therefore a longer response time ($\tau = Q/\pi f$) of the CPAS spectrophone. However, in most cases the QEPAS detection sensitivity for slow relaxing molecules can be improved by adding a molecular species such as water [21, 93, 101] or sulfur hexafluoride [20], which eliminates the V–T relaxation bottleneck.

4.2.4 Cavity-Enhanced Direct Frequency-Comb Spectroscopy (CE–DFCS)

A promising approach that addresses the issues of spectral coverage and analysis of multiple species while retaining the high spectral resolution and light intensity of lasers is DFCS [107]. The technique utilizes mode-locked lasers, which emit a train of ultrashort (< 100 femtoseconds (fs)) optical pulses that, in the frequency domain, corresponds to a discrete comb of equally spaced and highly resolved lines. This relationship is illustrated in Figure 4.6. The specific frequencies of the comb, ν_m , are given by the equation

$$\nu_m = m f_{rep} + f_0 \quad (4.6)$$

where the comb repetition rate f_{rep} is related to the pulse envelope spacing τ by

$$f_{rep} = \frac{1}{\tau} \quad (4.7)$$

and the comb offset frequency f_0 is determined by the phase shift $\Delta\Theta_{ce}$ of the underlying electromagnetic wave between successive pulses,

$$f_0 = \frac{\Delta\Theta_{ce} \cdot f_{rep}}{2\pi} \quad (4.8)$$

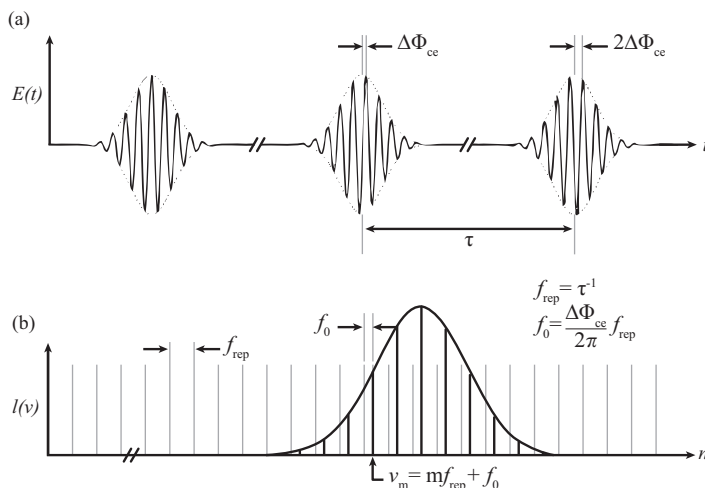


Figure 4.6 Time- (a) and frequency- (b) domain pictures of the generation of a frequency comb from a train of fs pulses from a mode-locked laser. Reprinted from [51] with permission from Annual Reviews, Inc.

The individual combs sample within the absorption profile of individual analyte transitions, and the bandwidth that can be covered is limited only by the output of the fs laser, which can be as broad as hundreds of nm. As f_{rep} and f_0 are radio frequencies, they can be directly measured and thus provide a means for extremely accurate optical frequency measurements. Applications of the technique to atomic and molecular spectroscopy in the near-infrared began in 2004 [108]. More recent developments which expand the capability of the technique for trace gas analysis are (1) expansion of the spectral coverage from the near-infrared into the mid-infrared and (2) integration of high finesse cavity enhancement [51, 55].

Initial reports of DFCS for molecular spectroscopy utilized a Ti:sapphire laser, which has direct frequency output of 0.7–0.9 μm . Thus, spectroscopy involved analysis of vibrational overtones of small molecules, for example acetylene, oxygen, water, and ammonia [109]. Coverage farther into the near-infrared (1.5–1.7 μm) was later obtained with Er-doped fiber lasers [55], with analysis of overtones of methane, ethane, carbon dioxide, carbon monoxide, and ammonia. Extension of this technique to the mid-infrared (2.5–12 μm) will take advantage of the roughly 100 fold enhancement of the spectral line intensity of fundamental rotational-vibrational transitions. Although fs lasers cannot access this region directly, nonlinear optical conversion techniques are relatively efficient due to the short time scale and large

peak power of the pulses. Both difference frequency generation (DFG) and optical parametric oscillators (OPO) have been applied to DFCS in the mid infrared spectral region. OPOs have the advantage of higher output powers, which is critical given that the power is distributed over many thousands of comb lines. For example, a Yb fiber based OPO was used to obtain powers of one watt from 2100 cm^{-1} to 3600 cm^{-1} . With this light the DFCS technique was demonstrated for analysis of nitrous oxide, methane, and a mixture of formaldehyde, methanol, and water vapor in nitrogen [54].

The infrared light can be readily incorporated into a multipass cell [54], but the greatest sensitivity enhancements will come from the use of a high finesse cavity. However, it is not possible to couple the entire bandwidth of the comb into the cavity at one time, due to intracavity dispersion, which results in an increasing mismatch between comb and cavity modes as one deviates from the center frequency of the cavity, f_{FSR} [51]. The optimum match is obtained when the frequency comb repetition rate and offset are adjusted to f_{FSR} . Locking the laser and cavity modes permits maximum power throughput, although only a subset of the original comb spectrum will be transmitted. Alternatively, dithering the laser (or cavity) modes allows the entire comb to be transmitted through the cavity, although at the cost of a longer duty cycle and lower average power. Ultimately, the bandwidth of the DFCS platform will be determined by the frequency dependence of the cavity finesse, which is limited by materials considerations to $\sim \pm 15\%$ of the center wavelength of the mirror reflectivity.

Detection can be accomplished by a variety of methods, as summarized in Figure 4.7. Time based detection methods (Figure 4.7a–b) have been largely supplanted by frequency based detection (Figure 4.7c–d), which takes advantage of multiplex detection schemes. The specific frequency based method chosen is dependent on the configuration of the rest of the DFCS platform. For example, if the laser modes are dithered in order to obtain transmission of every comb mode through the cavity, then the detection mode depicted in Figure 4.7c is used. This mode combines high vertical dispersion of the transmitted light by an angled étalon (virtually imaged phased array, or VIPA) with horizontal dispersion of overlapping modes with a conventional grating and a two-dimensional array detection to permit a snapshot of the cavity transmittance. A detailed description of the technique, including conversion of the fringed two-dimensional image into a one-dimensional spectrum, is described by Thorpe et al. [55]. The $1.5\text{--}1.7\text{ }\mu\text{m}$ spectrum is imaged as $8 \times 25\text{ nm}$ sections, with spectral resolution of $0.025\text{--}0.03\text{ cm}^{-1}$. Absorption is determined from the difference between images of reference and sample gases. Note that while the optical arrangement is potentially compact, the high dispersion of the VIPA means that calibration and reproducibility are very sensitive to small changes in alignment. Also, the method is restricted to the visible and near-infrared regions where two-dimensional array materials exhibit a response.

The configuration shown in Figure 4.7d, in which the light is analyzed with a Fourier transform spectrometer (FTIR), is suitable for when the laser and cavity modes are actively locked, or if mid-infrared light is generated. Compared to conventional FTIR spectroscopy with a black body emitter, the relative brightness of the a high power OPO allows spectra to be acquired ~ 10 times faster [51]. Since a phase-

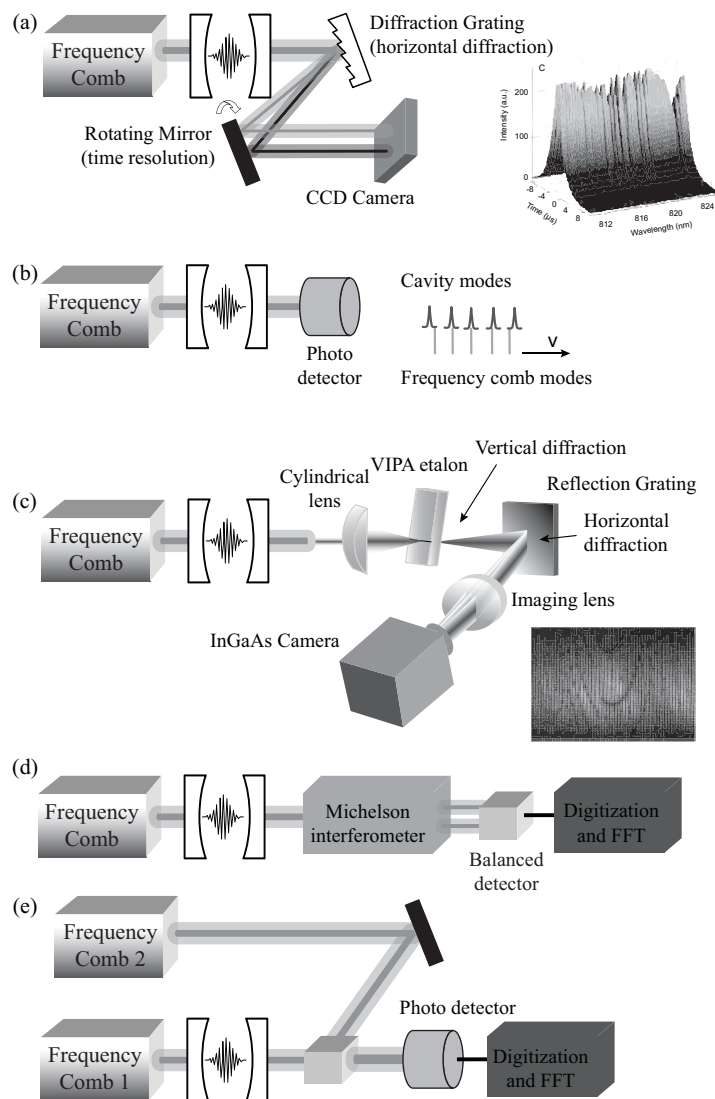


Figure 4.7 Detection schemes for cavity enhanced DFCS. (a) Ring down measurement, with horizontal frequency dispersion and vertical time dispersion provided by a rotating mirror. (b) Comb vernier spectroscopy, with time decay monitoring of a single selected comb line. (c) Two dimensional spectral resolution of multiple comb lines using a high dispersion VIPA and a grating for horizontal resolution of multiple modes. (d) FT spectroscopy of cavity locked comb lines. (e) Heterodyne detection of two comb sources. Techniques (c) and (d) are discussed in the text. Reprinted from [54] with permission from the Royal Society of Chemistry.

locked mid-infrared OPO emits a stable frequency comb, the addition of a high finesse femtosecond enhancement cavity for sample detection is feasible, which can further improve the detection sensitivity of the system [51, 55].

4.3 Applications of Semiconductor LAS Based Trace Gas Sensor Systems

The performance, cost and size of QCLs has generated considerable interest in developing LAS based gas sensor systems for a variety of commercial applications including industrial process monitoring [56, 110, 111, 124], pollution control monitoring [32, 33, 112, 113] and medical diagnostics [39, 114, 115, 116, 117, 118, 119, 120]. In this section we will provide a brief overview of the application of LAS based trace gas analyzer systems relevant to semiconductor and specialty gas monitoring.

4.3.1 OA–ICOS Online Measurement of Acetylene in an Industrial Hydrogenation Reactor

Ethylene is one of the most widely produced petrochemicals and is a key precursor used in a variety of important industrial products such as ethylene oxide, ethylene dichloride, polyethylene and other high volume derivatives [121]. Thus, careful control and optimization of the processes used to manufacture ethylene can provide significant economic advantages to the chemical industry. More than 97% of ethylene is produced by pyrolysis of hydrocarbons, i.e., thermal cracking of petrochemicals in the presence of steam, where acetylene can be a major byproduct or impurity of this process depending on the feedstock and quenching temperatures during the cracking process. In addition to causing a significant loss of product yield, acetylene acts as a poison to the end user's reaction catalyst used for manufacturing polyethylene and downstream end users of the final ethylene product typically require ≤ 2 ppmv of acetylene contamination for acceptance. Consequently, rapid, online monitoring of acetylene in both cracked gas and in the final ethylene product is important in olefin processing.

Currently, the standard analytical chemistry instrumentation used in the olefin industry to quantify acetylene in ethylene is gas chromatography (GC) coupled with flame ionization detection (FID) which provides measurement times up to ~ 600 seconds. In order to achieve real time process control and minimize process down time, an analyzer must provide much faster measurement rates (e.g., 1–30 seconds) while maintaining detection sensitivity and selectivity, which makes conventional GCs inadequate for this application. Micro-GCs with MEMS based separation columns and detectors have demonstrated acetylene detection in pure ethylene with measurement times of 20–40 seconds [122, 123]. No commercial deployment of such instruments has been reported. An alternate approach using a QCL based OA–ICOS system (Los Gatos Research, Inc., Mt. View, CA), has been successfully demonstrated for acetylene detection in a multi-component matrix from an olefin hydrogenation reactor [56, 124]. The system provides long effective optical pathlengths (e.g.,

typically 500–10,000 m) and maintains stable off-axis alignment that is essential for industrial applications.

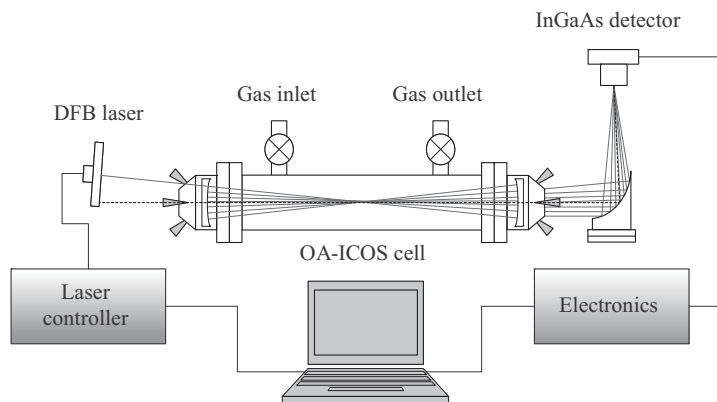


Figure 4.8 Schematic of an off-axis ICOS analyzer system.

A schematic of the Los Gatos Research OA-ICOS system implemented at the outlet of an industrial light hydrocarbon cracker is shown in Figure 4.8. The sensor employed a telecommunications grade, fiber coupled DFB diode laser producing 20–30 mW centered near 1531.6 nm. Laser control was accomplished using a custom laser driver card where the temperature and current could be controlled to within $\pm 0.01^\circ\text{C}$ and $\pm 0.1\text{ mA}$, sweeping $\sim 50\text{ GHz}$ in 0.01 seconds. The beam was launched into the cavity in an off-axis approach to probe the P(11) transition of the $\nu_1 + \nu_3$ band of $^{12}\text{C}_2\text{H}_2$. A custom amplified InGaAs detector with a gain of $3 \times 10^6\text{ V/A}$ and bandwidth of 30 kHz collected the light after traversing the cavity. One hundred transmission spectra were averaged (e.g., one second of data) to minimize measurement noise. A chemometric data analysis routine capable of simultaneously fitting several absorbing species was implemented and described in more detail by Le, et al. [56].

In high resolution diode laser applications, the intensity and shape of the absorbing features depends directly on the sample temperature and pressure and should be precisely controlled to match conditions under which calibration sets are obtained in order to maximize signal while maintaining adequate resolution between absorption spectra of the matrix. In this case, Le et al. surrounded the cavity with a heated, insulated blanket maintaining a sample temperature at $38 \pm 1^\circ\text{C}$. The sample pressure was controlled by a downstream pressure controller capable of maintaining the sample pressure range of 1.5–2.5 psi to within $\pm 0.02\text{ psi}$. Optimum temperature and pressure were determined by a series of comprehensive tests.

The sensor system was initially tested offline at the Dow Chemical Company's R&D laboratory (Freeport, TX) to empirically determine the system's performance specifications. The instrument's precision, detection limit and stability were evaluated by continuously monitoring a flowing acetylene standard. The analyzer demonstrated a 1σ measurement precision of better than $\pm 0.025\text{ ppmv}$ for a 40 hour period.

Table 4.1 Gas mixtures used to develop and validate chemometric calibration model. The mixtures span a wide range of anticipated process gas stream compositions. The acetylene concentrations of mixtures 1b, 5 and 6 were independently verified by the Dow Chemical Company. Reprinted from [56] with permission from the Society for Applied Spectroscopy.

Sample	Acetylene (ppmv)	Methyl acetylene (ppmv)	Ethylene (%)	Methane (%)	Ethane (%)
1	0.50	1017	40.1		
1b	0.50 (0.40)	1000	40.0		
2	0.96	3022	39.9		
3	1.48	5144	40.0		
4	1.50	990	40.0		
4b	1.50	1000	40.0		
5	2.86 (2.59)	1021	39.9		
6	8.0 (8.0)	999	40.1		
7	0.99	5024	40.0	20.0	30.0

Table 4.2 Measured values of several gas mixtures from both the OA–ICOS analyzer (6 second averaging) and a gas chromatograph. The gas chromatography data was obtained for a short-term study consisting of 30 consecutive analyses. Reprinted from [56] with permission from the Society for Applied Spectroscopy.

Acetylene					
BOC Reported (ppmv)	Off Axis ICOS (ppmv)	3 σ precision (\pm ppmv)		Accuracy/bias (\pm ppmv)	
		ICOS	GC	ICOS	GC
0.50	0.49	0.03	0.06	0.01	0.08
0.99	1.02	0.04	0.06	0.03	0.08
1.48	1.51	0.07	0.14	0.03	0.20
2.86	2.58	0.06	0.14	0.28	0.20
8.00	7.74	0.14	0.14	0.26	0.20
Methyl acetylene					
BOC Reported (ppmv)	OA–ICOS (ppmv)	3 σ precision (\pm ppmv)		Accuracy (%)	
1017	1020.9	5.8		0.4	
1021	1021.1	13.9		0.0	
3022	3082.3	63.0		2.0	
5349	5144.0	130.7		3.8	

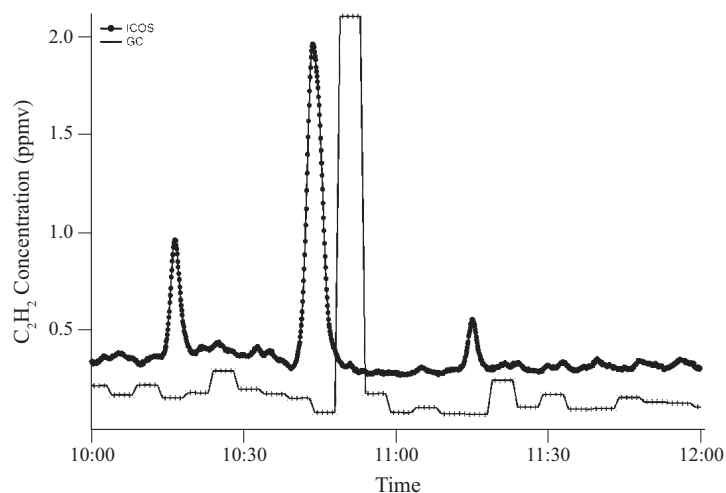


Figure 4.9 Measured online acetylene comparison data for OA-ICOS analyzer and GC. During fast acetylene fluctuations, the GC either misses such an event entirely or misreports it after completion. In contrast, the ICOS analyzer reports the acetylene data with good accuracy. Reprinted from [56] with permission from the Society for Applied Spectroscopy.

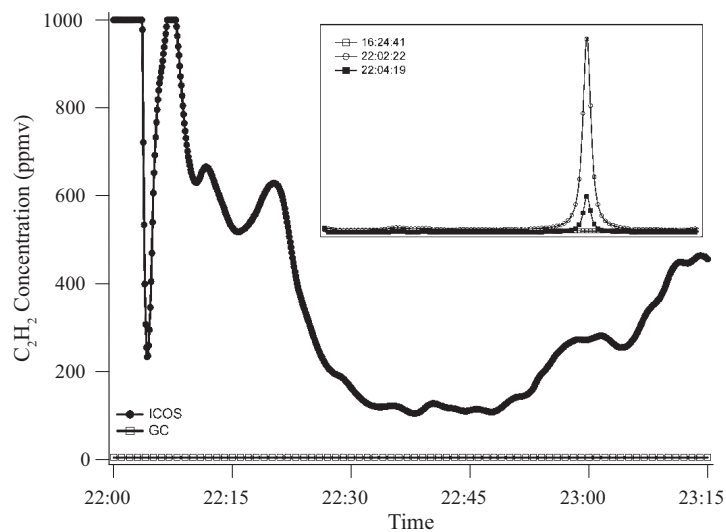


Figure 4.10 Demonstration of OA-ICOS analyzer to measure high concentration levels (~ 1000 ppmv) where the GC is limited to 10 ppmv. Inset depicts how the absorption spectra can be viewed for verification. The spectra indicate that the acetylene dip at 22:04 hours is a real process event. Reprinted from [56] with permission from the Society for Applied Spectroscopy.

Based on these measurements a detection limit of 0.050 ppmv in nitrogen was calculated on the basis of a signal-to-noise ratio of three. The accuracy of this instrument was further evaluated for seven mixtures prepared by the British Oxygen Company (BOC) that mimic typical plant operating conditions during steady state, alarm level and plant upset periods listed in Table 4.1. The mixtures were initially measured by BOC using GC with a relative uncertainty of $\pm 5\%$ for components < 5 ppmv and $\pm 2\%$ for components > 5 ppmv. Acetylene concentrations of three of the mixtures were verified by an optimized GC system at Dow Chemical Company and showed a slight deviation for samples 1b and 5. Additionally, the results of a successful comparison of the OA-ICOS system to typical online optimized GC monitoring at the Dow Chemical Company are summarized in Table 4.2. The slow response time of the GCs does not allow real time monitoring of methyl acetylene under process conditions and therefore no comparison data is available.

Following a successful laboratory demonstration, the OA-ICOS system was installed in a Dow hydrocarbon plant (Oyster Creek, TX) where it was operated in parallel with two pre-existing GC systems for five and a half months. Typical GC measurement times for acetylene and methyl acetylene were ~ 5 minutes and ~ 20 minutes, respectively. The OA-ICOS system routinely provided faster response times with comparable accuracy and, in some instances, tracked events that were too rapid for GC quantification as demonstrated in Figure 4.9. Subsequently Dow Chemical installed two OA-ICOS systems in a light hydrocarbon facility in Freeport, TX, and ran them in conjunction with newly installed GC systems capable of a 90 second measurement time. Results from the commercial implementation (Figure 4.10) showed that regardless of the GC response time, the OA-ICOS system out-performed the optimized GC system and correctly reflected actual variations in reactor outlet composition.

4.3.2 Multi-Component Impurity Analysis in Hydrogen Process Gas Using a Compact QEPAS Sensor

High purity hydrogen is used for various functions in semiconductor processing such as a cover gas for furnace processing, a carrier gas for transport of active doping agents or even reactive gas for material preparation. One such application is the microwave plasma-assisted low pressure chemical vapor deposition preparation of single-crystal diamond as a wide band-gap material via reaction of atomic hydrogen and a methyl radical [125]. To manufacture the diamond, high purity hydrogen, methane, and argon are flowed through a chamber containing the deposition substrate. A 2.45 GHz microwave plasma is used to generate atomic hydrogen, which reacts with methane to yield a methyl radical and hydrogen gas. The carbon containing radical then deposits onto the substrate as crystalline diamond. Improvements in the electronic properties of the single-crystal diamond can be directly attributed to enhanced crystalline quality and reduced defect concentration, which requires tight controls on the process gas mixtures and impurities formed in the processing, such as ammonia. Therefore, online monitoring of methane in the presence of hydrogen with simultaneous detection of impurity formation is a critical need for this process. The

utility of a LAS based sensor system employing a QCL for multi-component process monitoring was demonstrated as a QEPAS sensor system designed for detection of ammonia and methane in a hydrogen carrier gas [126].

The QEPAS technique presents a unique, new methodology for impurity analysis within hydrogen gas streams. An image of the QEPAS detection module is shown in Figure 4.11. As discussed in section 4.2.3, the microresonator (mR) plays a crucial role in QEPAS sensors and acts similarly to the acoustic resonator in conventional PAS [72]. The reported speed of sound in hydrogen is 1330 m/s at room temperature [127] which is ~ 4 times faster than in air, since the density of hydrogen is only $1/14^{\text{th}}$ of the density of air. The parameters and the performance of the mR are strongly dependent on the properties of the carrier gas, in particular the gas density and speed of sound within the gas. Thus, for this application the optimum length of the mR was calculated to be ~ 20 mm or ~ 40 mm when accounting for the length of both mRs. This increased mR length presents a challenge to focus the excitation diode laser beam passing through the 40 mm long mR and the 300 μm gap between the prongs of the QTF without optical contact. In fact, any optical contact between the diode laser excitation radiation and the mR or QTF results in an undesirable, non-zero background, which is several to a few tens of times larger than the thermal noise level of QEPAS [101]. As a result, the ~ 20 mm optimized mR tube length (which must be matched to the acoustic wavelength so that the acoustic energy can be efficiently accumulated in the mR tube) was not found suitable for QEPAS based trace gas detection in hydrogen. However, in previous QEPAS based sensor studies, it was observed that a non-matched short length mR can still increase the QEPAS sensitivity by a factor of ten times or more [98]. In this case, the mR tubes act to confine the sound wave, but do not exhibit a well defined resonant behavior. Therefore a non-matched mR configuration was adopted for the QEPAS based sensor where two, 5 mm long mR tubes, whose length is four times smaller than the evaluated 20 mm optimum length, were employed. The mR tubes featured an inner tube diameter of 0.58 mm and outer tube diameter of 0.9 mm similar to the design shown in Figure 4.5b.

The schematic diagram of the multi-component QEPAS sensor system shown in Figure 4.12 consists of three parts: 1) A control electronics unit (CEU), 2) an acoustic detection module (ADM), and 3) a switching module. The diode laser for ammonia detection (JDS Uniphase CQF 935.908-19570) along with two reference cells (Wavelength References, Inc.) were mounted inside the CEU, while the diode laser for methane detection (NEL, NLK1U5FAAA) and a four by four MEMS optical switch were mounted in the switching module. The CEU was responsible for measuring the QTF parameters, modulating the two diode laser at half resonant frequency of the QTF frequency and locking of the laser wavelength to a selected absorption line of the target analyte. The MEMS switch was controlled to direct either of the two diode lasers to the ADM via a parallel four bit binary code provided by the CEU. The sensor head consisted of the ADM, ultra small temperature, pressure and humidity sensors mounted inside of a compact enclosure. A notebook PC communicated with the CEU via a RS232 serial port for collection of the $2f$ harmonic data and gas temperature, pressure and humidity parameters. Sensitivity optimization of the sen-

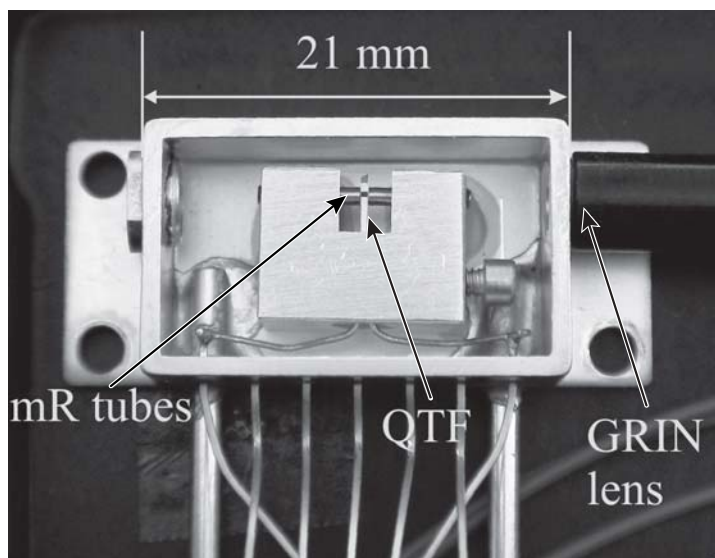


Figure 4.11 Fiber-coupled QEPAS ADM. With kind permission from Springer Science+Business Media: [126], fig. 1.

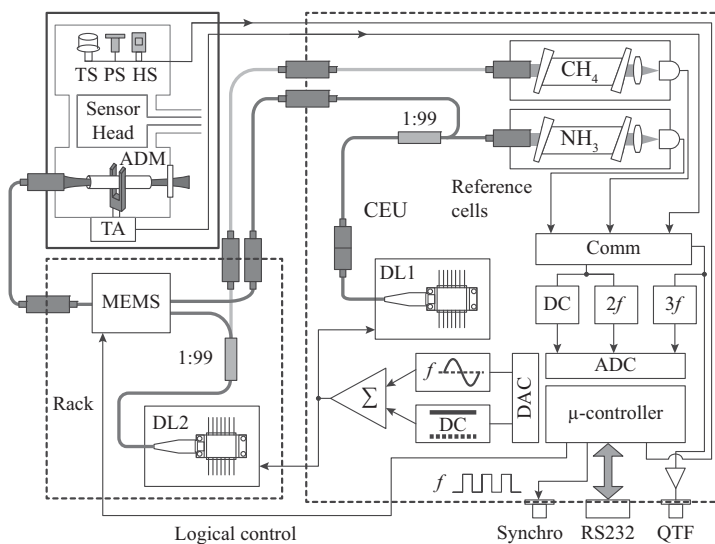


Figure 4.12 Schematic of a compact two gas QEPAS sensor. TS, PS, HS: temperature, pressure, and humidity sensors, ADM: acoustic detection module, TA: transimpedance amplifier, DL1, DL2: diode lasers, CEU: control electronics unit. With kind permission from Springer Science+Business Media: [126], fig. 2.

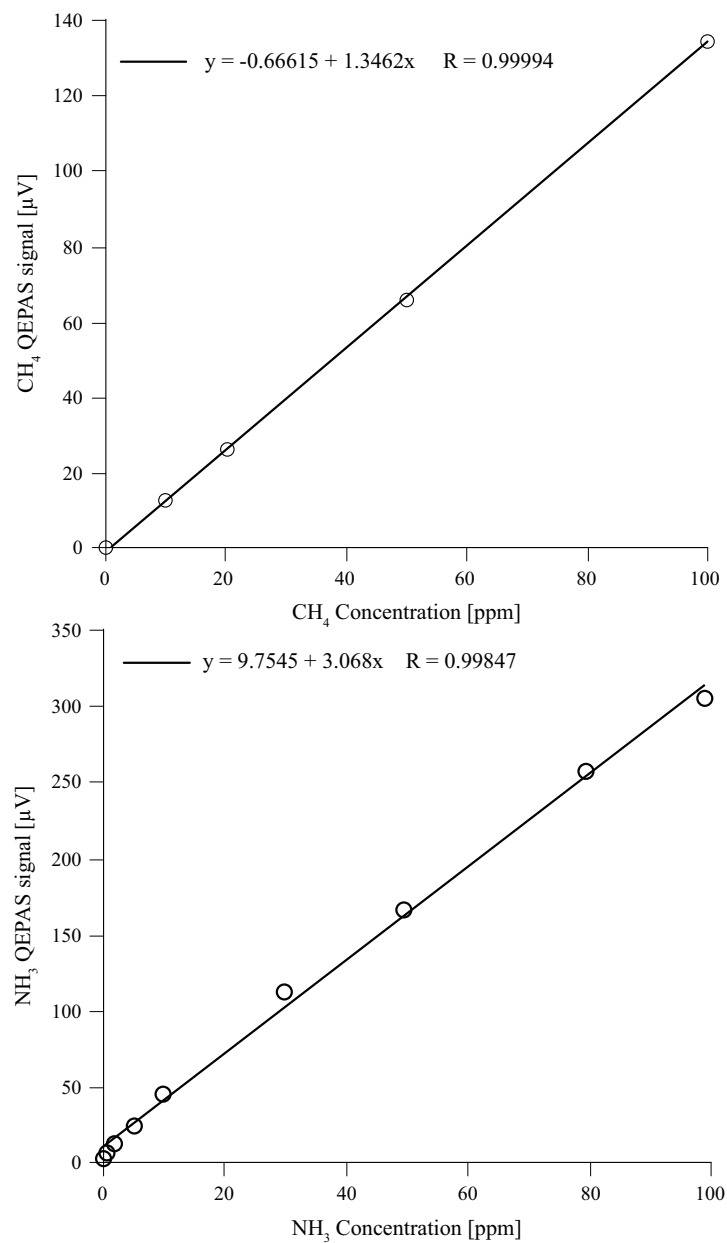


Figure 4.13 Plot of QEPAS response to different concentrations of certified (a) methane and (b) ammonia gas cylinders at the optimum pressure for each respective gas, i.e., 200 Torr for methane and 50 Torr for ammonia. With kind permission from Springer Science+Business Media: [126], figs. 7b and 11b.

sensor system was carried out to determine the effect of pressure on the molecular line broadening coefficient which determines the optimum laser wavelength modulation amplitude. For methane detection, the $2\nu_3$ band near 6057.1 cm^{-1} was employed while for ammonia detection a water and carbon dioxide interference free transition at 6528.76 cm^{-1} was selected. A maximum signal for methane and ammonia was observed at 200 Torr and 50 Torr, respectively; however, when the two gases were measured simultaneously, a pressure of 100 Torr was used causing a decrease in SNR of $\sim 8\%$ for each analyte. Sensor linearity and sensitivity were investigated for both molecules at their optimum pressure conditions and plotted in Figure 4.13. Based on these experiments, noise equivalent detection limits for methane and ammonia were calculated to be 3.2 ppmv and 1.27 ppmv, respectively, with a one second averaging time. The addition of water vapor did not significantly promote vibrational relaxation of methane, although a slight correction to the measured methane concentration was necessary by monitoring the moisture content. In addition, most industrial processes allow for longer measurement times. Therefore, the long term stability of the instrument was characterized by measuring the Allan variance of the ammonia channel shown in Figure 4.14. The data indicated that the sensor system followed a $1/\sqrt{t}$ dependence [34]. However, the Allan deviation started to drift when averaging exceeded 600 seconds. Hence, by signal averaging between 200–600 seconds, a detection sensitivity of 100–150 ppbv can be achieved. Further improvements of the detection sensitivity can be achieved by using higher power diode laser sources or fiber amplified diode lasers.

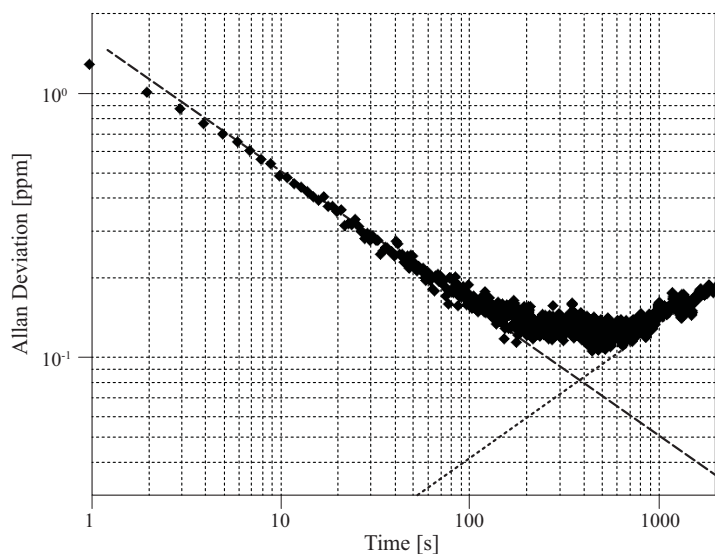


Figure 4.14 Allan deviation plotted as a function of the data averaging period. Solid circles trace: laser is locked to the ammonia absorption line, data acquisition time 1 s. Dashed line: $1/\sqrt{t}$ slope. Dotted line: \sqrt{t} slope. With kind permission from Springer Science+Business Media: [126], fig. 12.

4.3.3 Analysis of Trace Impurities in Arsine by CE-DFCS at 1.75–1.95 μm

Low concentrations of impurities in source materials can have detrimental effects on the physical properties of semiconductors. For example, III-V semiconductors made from arsine and phosphine will be degraded if water or oxygen concentrations of $\leq 10^{-8}$ (mol/mol) are present [53, 111]. At these concentration levels, oxygen acts as a dopant which creates additional energy levels in the semiconductor bandgap. Similar content levels must be managed for other impurities, such as hydrocarbons, carbon monoxide, carbon dioxide, and silicon and sulfur containing molecules [110]. Accurate detection of impurities at these levels is challenging and requires the development of new analytical techniques, especially for online monitoring during the growth phase.

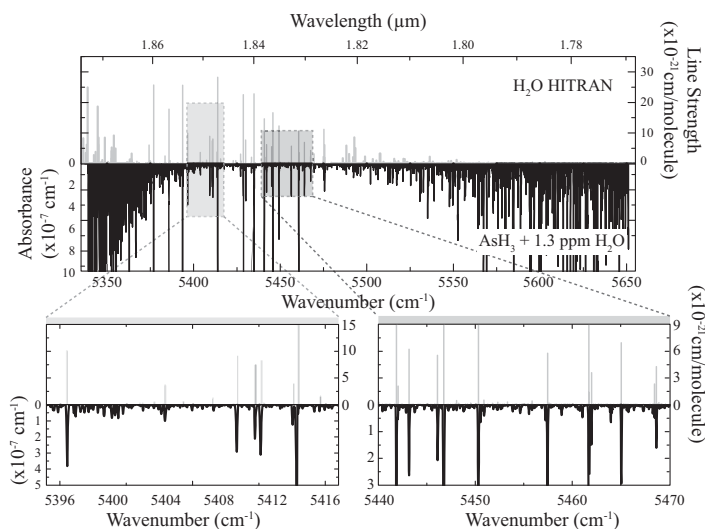


Figure 4.15 CE-DFCS spectra of arsine + 1.3 ppm water. Gray lines (extending upwards) are water transitions from the HITRAN database. Black lines (extending downwards) are the observed spectra. Insets show the coincidence of the observed and reference lines in the arsine spectral transparency window. With kind permission from Springer Science+Business Media: [53], fig. 2.

Cavity enhanced direct frequency-comb spectroscopy is an attractive candidate for this type of application, due to both its potential for sensitive measurements and its ability to access a broad spectral region with a single laser. These features are shown in a recent demonstration of the detection of trace levels of water in arsine [53]. Arsine is a difficult matrix for water detection due to its congested and extensive vibrational spectrum. However, there is a window in the arsine (arsine spectrum between 5400–5500 cm^{-1} (1.82–1.85 μm) in which water lines may be observed and quantified (see Figure 4.15).

A schematic of the experimental setup is shown in Figure 4.16. The output of a mode-locked Erbium-doped fiber ring laser (130 mW at 250 MHz) is amplified in a single mode highly nonlinear fiber amplifier (HNLF), yielding 81 fs pulses with 400 mW average power. The output is then broadened in a highly nonlinear silica fiber to generate spectral comb output in the region $4700\text{--}8300\text{ cm}^{-1}$ ($1.2\text{--}2.1\text{ }\mu\text{m}$). The light was coupled into a high finesse (peak $F = 30,000$) Fabry–Perot cavity with one, 2 m radius concave mirror and one flat mirror. The cavity length of $\sim 60\text{ cm}$ was adjusted to match the FSR to the comb repetition rate. The center wavelength of the cavity bandpass was $\sim 1.85\text{ }\mu\text{m}$, with a bandwidth of $\sim 200\text{ nm}$. The comb modes were dithered to overcome mode transmission issues associated with cavity dispersion. The cavity output is detected using a two dimensionally dispersive VIPA spectrometer, with a 320×256 pixel indium antimonide (InSb) plane array detector. The spectrometer has a resolution of 0.031 cm^{-1} and can cover 50 cm^{-1} in a single image. Absorption spectra were obtained by alternating acquisitions of 20 sample and 20 reference gas transmission images (for a 150 ms integration time per image), with additional averaging as required. Total scanning time for a 700 cm^{-1} spectrum was ~ 2.5 hours, with additional time required to exchange sample and reference gases. The typical total gas pressure in the cavity was 200 Torr.

With this system, Cossel et al. demonstrated trace detection of carbon dioxide, methane, hydrogen sulfide (manufacturer sample, $10\text{ ppmv} \pm 10\%$ each) and water

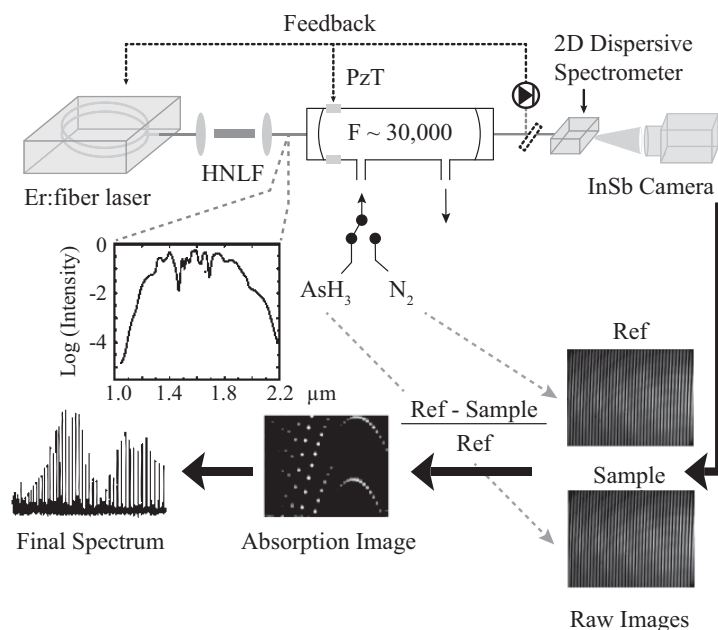


Figure 4.16 Schematic of CE-DFCS experimental platform. With kind permission from Springer Science+Business Media: [129], fig. 2.

(2.5 ppmv) in nitrogen, and trace water in arsine [53]. For such a sample, concentrations of the manufacturer supplied gases were determined within the specified uncertainty, and water was observed at 2.50 ± 0.12 ppm. Minimum detectable concentrations, based on the strongest lines in this spectral region, were: carbon dioxide, 325 ppmv; methane, 700 ppbv; hydrogen sulfide, 370 ppmv; water, 7 ppbv. For water, the range for linear measurement response extends over four orders of magnitude (7 ppbv–100 ppmv).

As seen in Figure 4.15, the arsine background is strong below 5400 cm^{-1} and above 5500 cm^{-1} . In this spectral region, the methane transitions occur between $5500\text{--}5700\text{ cm}^{-1}$, for hydrogen sulfide between $5050\text{--}5250\text{ cm}^{-1}$, and for carbon dioxide between $5050\text{--}5130\text{ cm}^{-1}$. Transitions for these molecules are obscured by arsine, and another spectral region is required for this application. The $5400\text{--}5500\text{ cm}^{-1}$ window coincides with strong water lines. Figure 4.15 shows the coincidence of observed water lines (black/down) with lines from the HITRAN database (gray/up), and there are several lines which are distinguishable from the arsine background. Using these lines, the concentration in the sample was measured to be 1.26 ± 0.08 ppmv with an integration time of 600 seconds. From the spectral quality, a detection limit of 31 ppmv was calculated for this matrix.

To make the system more suitable for field (industrial) applications, it was noted that the following improvements could be implemented. Acquisition time can be decreased by setting up a double beam configuration for simultaneous measurement of the sample and reference images. This would eliminate issues associated with gas delivery to and exchange in the cavity. Extension into other areas of the spectrum ($1.2\text{--}1.75$ and $1.95\text{--}2.1\text{ }\mu\text{m}$) should be possible with the supercontinuum output of the Er:fiber laser, which would allow the use of stronger lines and spectral regions where background interference might not exist.

4.4 Conclusions and Future Trends

Spectroscopic techniques that include semiconductor based laser absorption spectroscopy (LAS), cavity ring down spectroscopy (CRDS), integrated cavity output spectroscopy (ICOS), conventional and quartz enhanced photoacoustic spectroscopy (CPAS and QEPAS), evanescent wave spectroscopy, laser induced breakdown spectroscopy (LIBS), noise immune cavity enhanced optical heterodyne molecular spectroscopy (NICE-OHMS), cavity-enhanced optical frequency comb spectroscopy (CE-OFCS) have become important as scientific and industrial techniques. Laser absorption spectroscopy has benefited significantly from the development of infrared laser sources that can access the desired near-infrared and mid-infrared wavelengths, novel measurement techniques improved data acquisition and reduction methods. The choice of a specific spectroscopic measurement method is determined by the application as well as the commercial availability of semiconductor lasers such as QCLs, ICLs and LDs with powers of $> 20\text{ mW}$ and operating lifetimes comparable to near-infrared laser diodes (~ 10 years). Furthermore, improvements and innovations in LAS, CRDS, ICOS, QEPAS and DFCS sensor platforms, in particular more stable,

mass produced optical/mechanical designs as well as data acquisition and reduction techniques will lead to infrared semiconductor laser based instruments that can be operated by non-technical personnel and be manufactured at costs leading to sensor networks that permit both temporal and spatial trace gas monitoring.

Autonomously operated compact, reliable, real time, sensitive ($< 10^{-4}$), and highly selective ($< 3\text{--}500$ MHz) trace gas sensors based on various spectroscopic techniques using QCLs, ICLs and LDs have been demonstrated to be effective in numerous real world and fundamental science applications. While the focus of this chapter has been limited to LAS based sensors used in specialty and electronic gases such as chemical analysis and/or process control for manufacturing processes (e.g., petrochemical processing and exploration, alternative energy technologies and production, semiconductor wafer manufacture, pharmaceutical, metal processing, nuclear safeguards and food and beverage industries), QCL, ICL and LD based sensors have been applied to a wide range of politically and economically important areas. These include such diverse fields as atmospheric chemistry and environmental monitoring (e.g., carbon monoxide, carbon dioxide, methane and formaldehyde are important carbon gases in global warming), ozone depletion studies, acid rain, photo smog formation), industrial emission measurements (e.g., quantification of smokestack emissions, fence line perimeter monitoring by the petrochemical industry, combustion incinerators, down hole gas monitoring, gas pipeline and industrial plant safety), urban (e.g., automobile, truck, aircraft, marine and electrical power generation) and rural emissions (e.g., horticultural greenhouses, fruit storage and rice agro-ecosystems). Furthermore these types of sensors will also have a large impact on human health with applications in biomedical and the life sciences, such as non-invasive medical diagnostics that involves the detection and monitoring of numerous exhaled breath biomarkers (e.g., nitrogen oxide, carbon monoxide, carbon dioxide, ammonia, ethane and acetone). With the development of efficient mid-infrared lasers [7, 10, 128, 129, 130], we envision a significantly improved performance coupled with a reduction in size and cost of thermoelectrically cooled semiconductor laser based trace gas monitors that will lead to rapid increases in the implementation of sensor networks in many applications [112, 113].

REFERENCES

1. Faist, J., Capasso, F., Sivco, D. L., Hutchinson, A. L., & Cho, A. Y. (1994). Quantum cascade laser. *Science*, 264, 553–556.
2. Meyer, J. R., Vurgaftman, I., Yang, R. Q., & Ram-Mohan, L. R. (1996). Type-II and type-I interband cascade lasers. *Electronics Letters*, 32, 45–46.
3. Yang, R. Q. (1995). Infrared laser based on intersubband transitions in quantum wells. *Superlattices and Microstructures*, 17, 77–83.
4. Bismuto, A., Beck, M., & Faist, J. (2011). High power Sb-free quantum cascade laser emitting at $3.3\text{ }\mu\text{m}$ above $350\text{ }^{\circ}\text{K}$. *Applied Physics Letters*, 98, 19, 191104.
5. Capasso, F. (2010). High-performance mid-infrared quantum cascade lasers. *Optical Engineering*, 49, 11, 111102.

6. Gupta, J. A., Ventrudo, B. F., Waldron, P., & Barrios, P. J. (2010). External cavity tunable type-I diode laser with continuous-wave singlemode operation at 3.24 μm . *Electronics Letters*, 46, 1218–1220.
7. Razeghi, M., Bai, Y., Slivken, S., & Darvish, S. R. (2010). High-performance InP-based midinfrared quantum cascade lasers at Northwestern University. *Optical Engineering*, 49, 111103.
8. Vurgaftman, I., Kim, M., Kim, C. S., Bewley, W. W., Canedy, C. L., Lindle, J. R., . . . & Meyer, J. R. (2010). Challenges for mid-IR interband cascade lasers. *Proceedings of the SPIE*, 7616, 761619.
9. Zeller, W., Naehle, L., Fuchs, P., Gerschuetz, F., Hildebrandt, L., & Koeth, J. (2010). DFB lasers between 760 nm and 16 μm for sensing applications. *Sensors*, 10, 2492–2510.
10. Curl, R. F., Capasso, F., Gmachl, C., Kosterev, A. A., McManus, B., Lewicki, R., Pushkarsky, M., . . . Tittel, F. K. (2010). Quantum cascade lasers in chemical physics. *Chemical Physics Letters*, 487, 1–3, 1–18.
11. Kosterev, A. A., & Tittel, F. K. (2002b). Chemical sensors based on quantum cascade lasers. *Quantum Electronics, IEEE Journal of*, 38, 582–591.
12. McManus, J. B., Zahniser, M. S., Nelson, J. D. D., Shorter, J. H., Herndon, S., Wood, E., & Wehr, R. (2010). Application of quantum cascade lasers to high-precision atmospheric trace gas measurements. *Optical Engineering*, 49, 111124–11.
13. Lee, B., Wood, E., Zahniser, M., McManus, J., Nelson, D., Herndon, S., . . . Munger, J. (2011). Simultaneous measurements of atmospheric HONO and NO₂ via absorption spectroscopy using tunable mid-infrared continuous-wave quantum cascade lasers. *Applied Physics B: Lasers & Optics*, 102, 417–423.
14. Lewicki, R., Kosterev, A. A., Thomazy, D. M., Risby, T. H., Solga, S., Schwartz, T. B., & Tittel, F. K. (2011). Real time ammonia detection in exhaled human breath using a distributed feedback quantum cascade laser based sensor. *Proc. of SPIE* 7945, 50K–2.
15. Weidmann, D., Wysocki, G., Oppenheimer, C., & Tittel, F. K. (2005). Development of a compact quantum cascade laser spectrometer for field measurements of CO₂ isotopes. *Applied Physics B: Lasers & Optics*, 80, 255–260.
16. Kosterev, A. A., Malinovsky, A. L., Tittel, F. K., Gmachl, C., Capasso, F., Sivco, D. L., . . . Cho, A. Y. (2001). Cavity ringdown spectroscopic detection of nitric oxide with a continuous-wave quantum-cascade laser. *Applied Optics*, 40, 5522–5529.
17. Bakhirkin, Y. A., Kosterev, A. A., Curl, R. F., Tittel, F. K., Yarekha, D. A., Hvozdar, L., Giovannini, M., & Faist, J. (2006). Sub-ppbv nitric oxide concentration measurements using CW thermoelectrically cooled quantum cascade laser-based integrated cavity output spectroscopy. *Applied Physics B: Lasers & Optics*, 82, 149–154.
18. McCurdy, M. R., Bakhirkin, Y., Wysocki, G., & Tittel, F. K. (2007b). Performance of an exhaled nitric oxide and carbon dioxide sensor using quantum cascade laser-based integrated cavity output spectroscopy. *Journal of Biomedical Optics*, 12.
19. Dong, L., Lewicki, R., Liu, K., Tittel, F. K., Buerki, P. R., & Weida, M. J. (2012). Ultra-sensitive carbon monoxide detection by using EC-QCL based quartz-enhanced photoacoustic spectroscopy. *Applied Physics B: Lasers and Optics*, 107, 2, 275–283.
20. Kosterev, A. A., Bakhirkin, Y. A., & Tittel, F. K. (2005a). Ultrasensitive gas detection by quartz-enhanced photoacoustic spectroscopy in the fundamental molecular absorption bands region. *Applied Physics B: Lasers & Optics*, 80, 133–138.

21. Kosterev, A. A., Wysocki, G., Bakhirkin, Y. A., So, S., Lewicki, R., Fraser, M., Tittel, F., & Curl, R. F. (2008). Application of quantum cascade lasers to trace gas analysis. *Applied Physics B: Lasers & Optics*, 90, 165–176.
22. Kosterev, A. A., Dong, L., Thomazy, D., Tittel, F., & Overby, S. (2010b). QEPAS for chemical analysis of multi-component gas mixtures. *Applied Physics B: Lasers & Optics*, 101, 649–659.
23. Lewicki, R., Wysocki, G., Kosterev, A. A., & Tittel, F. K. (2007b). QEPAS based detection of broadband absorbing molecules using a widely tunable, CW quantum cascade laser at 8.4 μm . *Optics Express*, 15, 7357–7366.
24. Zaugg, C. A., Lewicki, R., Day, T., Curl, R. F., & Tittel, F. K. (2011). Faraday rotation spectroscopy of nitrogen dioxide based on a widely tunable external cavity quantum cascade laser. *Proceedings of SPIE* 7945, 500–1.
25. Welzel, S., Hempel, F., Hübner, M., Lang, N., Davies, P. B., & Röpcke, J. (2010). Quantum cascade laser absorption spectroscopy as a plasma diagnostic tool: An overview, *Sensors*, 10, 6861–6900.
26. Belenky, G., Shterengas, L., Kipshidze, G., & Hosoda, T. (2011). Type-I diode lasers for spectral region above 3 μm . *IEEE Journal on Selected Topics in Quantum Electronics*, 17, 5, 1426–1434.
27. Christensen, L. E., Mansour, K., & Yang, R. Q. (2010). Thermoelectrically cooled interband cascade laser for field measurements. *Optical Engineering*, 49, 11, 111119.
28. Kosterev, A. A., Bakhirkin, Y. A., Tittel, F. A., McWhorter, S., Ashcraft, D. (2008). QEPAS methane sensor performance for humidified gases. *Applied Physics B: Lasers & Optics*, 92, 103–109.
29. Schilt, S., Thévenaz, L., & Robert, P. (2003). Wavelength modulation spectroscopy: Combined frequency and intensity laser modulation. *Applied Optics*, 42, 6728–6738.
30. Schilt, S., & Thévenaz, L. (2006). Wavelength modulation photoacoustic spectroscopy: Theoretical description and experimental results. *Infrared Physics & Technology*, 48, 154–162.
31. Fried, A., Sewell, S., Henry, B., Wert, B. P., Gilpin, T., & Drummond, J. R. (1997). Tunable diode laser absorption spectrometer for ground-based measurements of formaldehyde. *Journal Geophysics Res.*, 102(D5), 6253–6266.
32. Fried, A., Henry, B., Wert, B., Sewell, S., & Drummond, J. R. (1998). Laboratory, ground-based, and airborne tunable diode laser systems: Performance characteristics and applications in atmospheric studies. *Applied Physics B: Lasers & Optics*, 67, 317–330.
33. Fried, A., & Richter, D. (2007). Infrared absorption spectroscopy in analytical techniques for atmospheric measurement. In D. Heard (Ed.), *Analytical techniques for atmospheric measurement* (pp. 72–146). Blackwell Publishing.
34. Werle, P. (2011). Accuracy and precision of laser spectrometers for trace gas sensing in the presence of optical fringes and atmospheric turbulence. *Applied Physics B: Lasers & Optics*, 102, 313–329.
35. Zahniser, M. S., Nelson, D. D., McManus, J. B., Keabian, P. L., & Lloyd, D. (1995). Measurement of trace gas fluxes using tunable diode laser spectroscopy. *Philosophical Transactions: Physical Sciences and Engineering*, 351, 371–382.

36. McManus, J. B., Kebabian, P. L., & Zahniser, W. S. (1995). Astigmatic mirror multipass absorption cells for long-path-length spectroscopy. *Applied Optics*, 34, 3336–3348.
37. Rao, G. N., & Karpf, A. (2010). High sensitivity detection of NO₂ employing cavity ringdown spectroscopy and an external cavity continuously tunable quantum cascade laser. *Applied Optics*, 49, 4906–4914.
38. Tittel, F. K., Kosterev, A. A., Bakhirkin, Y. A., Roller, C. B., Weidmann, D., & Curl, R. F. (2002). Chemical sensors based on quantum cascade lasers. *IEEE Journal of Quantum Electronics*, 38, 582–591.
39. Bakhirkin, Y. A., Kosterev, A. A., Roller, C., Curl, R. F., & Tittel, F. K. (2004). Mid-infrared quantum cascade laser based off-axis integrated cavity output spectroscopy for biogenic nitric oxide detection. *Applied Optics*, 43, 11, 2257–2266.
40. Sonnenfroh, D. M., Rawlins, W. T., Allen, M. G., Gmachl, C., Capasso, F., Hutchinson, A. L., . . . Cho, A. Y. (2001). Application of balanced detection to absorption measurements of trace gases with room-temperature, quasi-cw quantum-cascade lasers. *Applied Optics*, 40, 812–820.
41. Gottfried, J., De Lucia, F., Munson, C., & Miziolek, A. (2009). Laser-induced breakdown spectroscopy for detection of explosives residues: a review of recent advances, challenges, and future prospects. *Analytical and Bioanalytical Chemistry*, 395, 283–300.
42. Foltynowicz, A., Schmidt, F. M., Ma, W., & Axner, O. (2008). Noise-immune cavity-enhanced optical heterodyne molecular spectroscopy: Current status and future potential. *Applied Physics B: Lasers & Optics*, 92, 313–326.
43. Ye, J., Ma, L.-S., & Hall, J. L. (1998). Ultrasensitive detections in atomic and molecular physics: demonstration in molecular overtone spectroscopy. *Journal of the Optical Society of America B*, 15, 6–15.
44. Ganser, H., Urban, W., & Brown, A. M. (2003). The sensitive detection of NO by Faraday modulation spectroscopy with a quantum cascade laser. *Molecular Physics*, 101, 545–550.
45. Lewicki, R., Doty, J. H., Curl, R. F., Tittel, F. K., & Wysocki, G. (2009). Ultrasensitive detection of nitric oxide at 5.33 μm by using external cavity quantum cascade laser-based Faraday rotation spectroscopy. *Proceedings of the National Academy of Sciences USA*, 106, 12587–12592.
46. Litfin, G., Pollock, C. R., Curl, R. F., & Tittel, F. K. (1980). Sensitivity enhancement of laser absorption spectroscopy by magnetic rotation effect. *Journal of Chemical Physics*, 72, 6602–6605.
47. Elia, A., Lugará, P. M., Di Franco, C., & Spagnolo, V. (2009). Photoacoustic techniques for trace gas sensing based on semiconductor laser sources. *Sensors*, 9, 616–628.
48. Lima, J. P., Vargas, H., Miklós, A., Angelmahr, M., & Hess, P. (2006). Photoacoustic detection of NO₂ and N₂O using quantum cascade lasers. *Applied Physics B: Lasers & Optics*, 85, 279–284.
49. Kosterev, A. A., & Tittel, F. K. (2004b). Ammonia detection by use of quartz-enhanced photoacoustic spectroscopy with a near-IR telecommunication diode laser. *Applied Optics*, 43, 6213–6217.
50. Kosterev, A. A., Tittel, F. K., Serebryakov, D. V., Malinovsky, A. L., & Morozov, I. V. (2005b). Applications of quartz tuning forks in spectroscopic gas sensing. *Review of Scientific Instruments*, 76, 43105.

51. Adler, F., Thorpe, M. J., Cossel, K. C., & Ye, J. (2010). Cavity-enhanced direct frequency comb spectroscopy: Technology and applications. *Annual Review of Analytical Chemistry*, 3, 175-205.
52. Adler, F., Maslowski, P., Foltynowicz, A., Cossel, K. C., Briles, T. C., Hartl, I., & Ye J. (2010b). Mid-infrared Fourier transform spectroscopy with a broadband frequency comb. *Optics Express*, 18, 21861.
53. Cossel, K. C., Adler, F., Bertness, K. A., Thorpe, M. J., Feng, J., Raynor, M. W., Ye, J. (2010). Analysis of trace impurities in semiconductor gas via cavity-enhanced direct frequency comb spectroscopy. *Applied Physics B: Lasers & Optics*, 100, 4, 917-924.
54. Foltynowicz, A., Masłowski, P., Ban, T., Adler, F., Cossel, K. C., Briles, T. C., Ye, J. (2011). Optical frequency comb spectroscopy. *Faraday Discussions*, 150, 23-31.
55. Thorpe, M. J., Balslev-Clausen, D., Kirchner, M. S., & Ye, J. (2008). Cavity-enhanced optical frequency comb spectroscopy: Application to human breath analysis. *Optics Express*, 16, 4, 2387-2397.
56. Le, L. D., Tate, J. D., Seasholtz, M. B., Gupta, M., Owano, T., Baer, D., . . . Zhu, J. (2008). Development of a rapid on-line acetylene sensor for industrial hydrogenation reactor optimization using off-axis integrated cavity output spectroscopy. *Applied Spectroscopy*, 62, 59-65.
57. Lee, B. G., Belkin, M. A., Audet, R., MacArthur, J., Diehl, L., Pflugl, C., & Capasso, F. (2007). Widely tunable single-mode quantum cascade laser source for mid-infrared spectroscopy. *Applied Physics Letters*, 91, 231101.
58. Caffey, D., Radunsky, M. B., Cook, V., Weida, M., Buerki, P. R., Crivello, S., & Day, T. (2011). Recent results from broadly tunable external cavity quantum cascade lasers. *Proceedings of SPIE Photonics West*, 7953-7954.
59. Busch, W. K., & Busch, A. M. (1999). Introduction to cavity-ringdown spectroscopy. In Kenneth W. Busch & Marianna A. Busch (Eds.), *Cavity-ringdown spectroscopy* (pp. 7-19). USA: Oxford University Press.
60. Paldus, B. A., & Kachanov, A. A. (2005). An historical overview of cavity-enhanced methods. *Canadian Journal of Physics*, 83, 975-999.
61. O'Keefe, A., & Deacon, D. A. G. (1988). Cavity ring-down optical spectrometer for absorption measurements using pulsed laser sources. *Reviews of Scientific Instruments*, 59, 2544-2551.
62. Ramponi, A. J., Milanovich, F. P., Kan, T., & Deacon, D. (1988). High sensitivity atmospheric transmission measurements using a cavity ringdown technique. *Applied Optics*, 27, 4606-4608.
63. Scherer, J. J., Paul, J. B., O'Keefe, A., & Saykally, R. J. (1997). Cavity ringdown laser absorption spectroscopy: History, development, and application to pulsed molecular beams. *Chemical Review*, 97, 25-51.
64. O'Keefe, A. (1998). Integrated cavity output analysis of ultra-weak absorption. *Chemical Physics Letters*, 293, 331-336.
65. O'Keefe, A., Scherer, J. J., & Paul, J. B. (1999). CW Integrated cavity output spectroscopy. *Chemical Physics Letters*, 307, 343-349.
66. Paldus, B. A., Harb, C. C., Spence, T. G., Zare, R. N., Gmachl, C., Capasso, F., . . . Cho, A. Y. (2000). Cavity ringdown spectroscopy using mid-infrared quantum-cascade lasers. *Optics Letters*, 25, 666-668.

67. Sukhorukov, O., Lytkine, A., Manne, J., Tulip, J., & Jager, W. (2006). Cavity ring-down spectroscopy with a pulsed distributed feedback quantum cascade laser. (R. Manijeh & J. B. Gail, Trans.). *SPIE*, 61270A.
68. Paul, J. B., Lapson, L., & Anderson, J. G. (2001). Ultrasensitive absorption spectroscopy with a high-finesse optical cavity and off-axis alignment. *Applied Optics*, 40, 4904–4910.
69. Engel, G. S., Drisdell, W. S., Keutsch, F. N., Moyer, E. J., & Anderson, J. G. (2006). Ultrasensitive near-infrared integrated cavity output spectroscopy technique for detection of CO at 1.57 μm : New sensitivity limits for absorption measurements in passive optical cavities. *Applied Optics*, 45, 9221–9229.
70. Sayres, D. S., Moyer, E. J., Hanisco, T. F., Clair, J. M., Keutsch, F. N., OBrien, A., ... & Anderson, J. G. (2009). A new cavity based absorption instrument for detection of water isotopologues in the upper troposphere and lower stratosphere. *Review of Scientific Instruments*, 80, 44102–44102.
71. Rao, G. N., & Karpf, A. (2011). Extremely sensitive detection of NO₂ employing off-axis integrated cavity output spectroscopy coupled with multiple line integrated absorption spectroscopy. *Applied Optics*, 50, 1915–1924.
72. Miklós, A., Hess, P., & Bozoki, Z. (2001). Application of acoustic resonators in photoacoustic trace gas analysis and metrology. *Review of Scientific Instruments*, 72, 1937–1955.
73. Rossi, A., Buffa, R., Scotoni, M., Bassi, D., Iannotta, S., & Boschetti, A. (2005). Optical enhancement of diode laser-photoacoustic trace gas detection by means of external Fabry-Perot cavity. *Applied Physics Letters*, 87, 041110.
74. Elia, A., Lugará, P. M., & Giancaspro, C. (2005). Photoacoustic detection of nitric oxide by use of a quantum-cascade laser. *Optics Letters*, 30, 988–990.
75. Hofstetter, D., Beck, M., Faist, J., Nägele, M., & Sigrist, M. W. (2001). Photoacoustic spectroscopy with quantum cascade distributed-feedback lasers. *Optics Letters*, 26, 887–889.
76. da Silva, M. G., Vargas, H., Miklós, A., & Hess, P. (2004). Photoacoustic detection of ozone using a quantum cascade laser. *Applied Physics B: Lasers & Optics*, 78, 6, 677–680.
77. Pushkarsky, M. B., Tsekoun, A., Dunayevskiy, I. G., Go, R., & Patel, C. K. N. (2006b). Sub-parts-per-billion level detection of NO₂ using room-temperature quantum cascade lasers. *Proceedings of the National Academy of Sciences USA*, 103, 10846–10849.
78. Rey, J. M., & Sigrist, M. W. (2008). New differential mode excitation photoacoustic scheme for near-infrared water vapour sensing. *Sensors and Actuators B: Chemical*, 135, 161–165.
79. Lee, C.-M., Bychkov, K. V., Kapitanov, V. A., Karapuzikov, A. I., Ponomarev, Y. N., Sherstov, I. V., & Vasiliev, V. A. (2007). High-sensitivity laser photoacoustic leak detector. *Optical Engineering*, 46, 064302.
80. Miklós, A., Hess, P., Mohacsi, A., Sneider, J., Kamm, S., & Schafer, S. (1999). Improved photoacoustic detector for monitoring polar molecules such as ammonia with a 1.53 μm DFB diode laser. *AIP Conference Proceedings*, 463, 126–128.
81. Bijnen, F. G. C., Reuss, J., & Harren, F. J. M. (1996). Geometrical optimization of a longitudinal resonant photoacoustic cell for sensitive and fast trace gas detection. *Review of Scientific Instruments*, 67, 8, 2914–2923.

82. Bernegger, S., & Sigrist, M. W. (1990). CO-laser photoacoustic spectroscopy of gases and vapours for trace gas analysis. *Infrared Physics*, 30, 5, 375–429.
83. Costopoulos, D., Miklós, A., & Hess, P. (2002). Detection of N₂O by photoacoustic spectroscopy with a compact, pulsed optical parametric oscillator. *Applied Physics B: Lasers & Optics*, 75, 2, 385–389.
84. Mukherjee, A., Prasanna, M., Lane, M., Go, R., Dunayevskiy, I., Tsekoun, A., & Patel, C. K. N. (2008). Optically multiplexed multi-gas detection using quantum cascade laser photoacoustic spectroscopy. *Applied Optics*, 47, 4884–4887.
85. Ng, J., Kung, A. H., Miklós, A., & Hess, P. (2004). Sensitive wavelength-modulated photoacoustic spectroscopy with a pulsed optical parametric oscillator. *Optical Letters*, 29, 1206–1208.
86. Pushkarsky, M. B., Webber, M. E., & Patel, C. K. N. (2003). Ultra-sensitive ambient ammonia detection using CO₂-laser-based photoacoustic spectroscopy. *Applied Physics B: Lasers & Optics*, 77, 381–385.
87. Pushkarsky, M. B., Dunayevskiy, I. G., Prasanna, M., Tsekoun, A. G., Go, R., & Patel, C. K. N. (2006a). High-sensitivity detection of TNT. *Proceedings of the National Academy of Sciences USA*, 103, 19630–19634.
88. Sigrist, M. W., & Thoeny, A. (1993). Atmospheric trace gas monitoring by CO₂ laser photoacoustic spectroscopy. (I. S. Harold and P. Ulrich, Trans.). *SPIE*, 174–184.
89. Webber, M. E., Pushkarsky, M., & Patel, C. K. N. (2003). Fiber-amplifier-enhanced photoacoustic spectroscopy with near-infrared tunable diode lasers. *Applied Optics*, 42, 2119–2126.
90. Kosterev, A. A., Bakhirkin, Y. A., Curl, R. F., & Tittel, F. K. (2002a). Quartz-enhanced photoacoustic spectroscopy. *Optics Letters*, 27, 1902–1904.
91. Wysocki, G., Kosterev, A. A., & Tittel, F. K. (2006). Influence of molecular relaxation dynamics on quartz-enhanced photoacoustic detection of CO₂ at $\lambda = 2 \mu\text{m}$. *Applied Physics B: Lasers & Optics*, 85, 301–306.
92. Petra, N., Zweck, J., Kosterev, A. A., Minkoff, S. E., & Thomazy, D. (2009). Theoretical analysis of a quartz-enhanced photoacoustic spectroscopy sensor. *Applied Physics B: Lasers & Optics*, 94, 673–680.
93. Lewicki, R., Wysocki, G., Kosterev, A. A., & Tittel, F. K. (2007a). Carbon dioxide and ammonia detection using 2 μm diode laser based quartz-enhanced photoacoustic spectroscopy. *Applied Physics B: Lasers & Optics*, 87, 157–162.
94. Liu, K., Guo, X. Y., Yi, H. M., Chen, W. D., Zhang, W. J., & Gao, X. M. (2009). Off-beam quartz-enhanced photoacoustic spectroscopy. *Optics Letters*, 34, 1594–1596.
95. Liu, K., Yi, H., Kosterev, A. A., Chen, W., Dong, L., Wang, L., . . . Gao, X. (2010). Trace gas detection based on off-beam quartz enhanced photoacoustic spectroscopy: Optimization and performance evaluation. *Review of Scientific Instruments*, 81, 103103.
96. Köhring, M., Pohlkötter, A., Willer, U., Angelmahr, M., & Schade, W. (2011). Tuning fork enhanced interferometric photoacoustic spectroscopy: A new method for trace gas analysis. *Applied Physics B: Lasers & Optics*, 102, 133–139.
97. Kosterev, A. A., & Doty III, J. H. (2010c). Resonant optothermoacoustic detection: Technique for measuring weak optical absorption by gases and micro-objects. *Optics Letters*, 35, 3571–3573.

98. Horstjann, M., Bakhirkin, Y. A., Kosterev, A. A., Curl, R. F., Tittel, F. K., Wong, C. M., Hill, C. J., & Yang, R. Q. (2004). Formaldehyde sensor using interband cascade laser based quartz-enhanced photoacoustic spectroscopy. *Applied Physics B: Lasers & Optics*, 79, 799–803.
99. Kosterev, A. A., Bakhirkin, Y. A., Tittel, F. K., Blaser, S., Bonetti, Y., & Hvozdar, L. (2004a). Photoacoustic phase shift as a chemically selective spectroscopic parameter. *Applied Physics B: Lasers & Optics*, 78, 673–676.
100. Kosterev, A. A., Mosely, T. S., & Tittel, F. K. (2006). Impact of humidity on quartz-enhanced photoacoustic spectroscopy based detection of HCN. *Applied Physics B: Lasers & Optics*, 85, 295–300.
101. Spagnolo, V., Kosterev, A., Dong, L., Lewicki, R., & Tittel, F. (2010). NO trace gas sensor based on quartz-enhanced photoacoustic spectroscopy and external cavity quantum cascade laser. *Applied Physics B: Lasers & Optics*, 100, 125–130.
102. Grober, R. D., Acimovic, J., Schuck, J., Hessman, D., Kindlemann, P. J., Hespanha, J., . . . Manus, S. (2000). Fundamental limits to force detection using quartz tuning forks. *Review of Scientific Instruments*, 71, 2776–2780.
103. Bauer, C., Willer, U., Lewicki, R., Pohlkötter, A., Kosterev, A., Kosynkin, D., . . . Schade, W. (2009). A Mid-infrared QEPAS sensor device for TATP detection. *Journal of Physics: Conference Series*, 157, 012002.
104. Bauer, C., Willer, U., & Schade, W. (2010). Use of quantum cascade lasers for detection of explosives: Progress and challenges. *Optical Engineering*, 49, 11, 111126.
105. Kosterev, A. A., Buerki, P., Dong, L., Reed, M., Day, T., & Tittel, F. (2010a). QEPAS detector for rapid spectral measurements. *Applied Physics B: Lasers & Optics*, 100, 173–180.
106. Wojcik, M. D., Phillips, M. C., Cannon, B. D., & Taubman, M. S. (2006). Gas-phase photoacoustic sensor at 8.41 μm using quartz tuning forks and amplitude-modulated quantum cascade lasers. *Applied Physics B: Lasers & Optics*, 85, 307–313.
107. Cundiff, S. T., Ye, J. (2003). Colloquium: Femtosecond optical frequency combs. *Reviews of Modern Physics*, 75, 1, 325–342.
108. Marian, A., Stowe, M. C., Lawall, J. R., Felinto, D., Ye, J. (2004). United time-frequency spectroscopy for dynamics and global structure. *Science*, 306, 2063–2068.
109. Thorpe, M. J., Moll, K. D., Jones, R. J., Safdi, B., Ye, J. (2006). Broadband cavity ringdown spectroscopy for sensitive and rapid molecular detection. *Science*, 311, 1595–1599.
110. Funke, H. H., Grissom, B. L., McGrew, C. E., Raynor, M. W. (2003). Techniques for the measurement of trace moisture in high-purity electronic specialty gases. *Review of Scientific Instruments*, 74, 3909–3933.
111. Lehman, S. K., Bertness, K. A., Hodges, J. T. (2003). Detection of trace water in phosphine with cavity ring-down spectroscopy. *Journal of Crystal Growth*, 250, 262–268.
112. So, S., Amiri Sani, A., Zhong, L., & Tittel, F. (2009). Laser spectroscopic trace-gas sensor networks for atmospheric monitoring applications. In ESSA Workshop 2009, San Francisco, California, USA.
113. So, S., Jeng, E., Smith, C., Krueger, D. & G., W. (2010). Next generation infrared sensor instrumentation: remote sensing and sensor networks using the open PHOTONS repository. (S. Marija & P. Gonzalo, Trans.). *SPIE*, 780818.

114. Cheng, W.-H., & Lee, W.-J. (1999). Technology development in breath microanalysis for clinical diagnosis. *Journal of Laboratory and Clinical Medicine*, 133, 3, 218–228.
115. Dweik, R. A., & Amann, A. (2008). Exhaled breath analysis: The new frontier in medical testing. *Journal of Breath Research*, 2.
116. McCurdy, M. R., Bakhirkin, Y., Wysocki, G., Lewicki, R., & Tittel, F. K. (2007a). Recent advances of laser-spectroscopy-based techniques for applications in breath analysis. *Journal of Breath Research* 1, 014001.
117. Mürtz, P., Menzel, L., Bloch, W., Hess, A., Michel, O., & Urban, W. (1999). LMR spectroscopy: a new sensitive method for on-line recording of nitric oxide in breath. *Journal of Applied Physiology*, 86, 1075–1080.
118. Mürtz, M., & Hering, P. (2008). Online monitoring of exhaled breath using mid-infrared laser spectroscopy. In Majid Ebrahim-Zadeh & Irina T. Sorokina (Eds.), *Mid-infrared Coherent Sources and Applications* (pp. 535–555). Springer: Netherlands.
119. Risby, T., & Tittel, F. K. (2010). Current status of mid-infrared quantum and interband cascade lasers for clinical breath analysis. *Optical Engineering*, 49, 111123.
120. Shorter, J. H., Nelson, D. D., McManus, J. B., Zahniser, M. S., & Milton, D. K. (2010). Multicomponent breath analysis with infrared absorption using room-temperature quantum cascade lasers. *Sensors Journal, IEEE*, 10, 76–84.
121. Lee, S. H. (2004). *Partial catalytic hydrogenation of acetylene in ethylene production*. Johor, Malaysia: KLM Technology Group. Retrieved from http://www.klmttechgroup.com/PDF/Articles/acetylene_converter.pdf
122. Manginell, R. P., Okandan, M., Kottentstette, R. J., Lewis, P. R., Adkins, D. R., Shul, R. J., Bauer, J. M., . . . Sokolowski, S. (2003). Monolithically-integrated microchemlab for gas-phase chemical analysis. *Proceedings of the u-TAS 2003 Workshop, Squaw Valley, California, September, 2003*, 1247–1250.
123. Robinson, A. (2003). Sandia microsensors for industrial process monitoring. *DOE Sensors and Automation FY03 Annual Review Meeting*. San Francisco, California.
124. Le, L. D., Tate, J. D., Seasholtz, M. B., Gupta, M., Baer, D., Knittel, T., . . . Zhu, J. (2006). Rapid online analysis of acetylene for improved optimization of hydrogenation reactors. *Proceedings of the 2006 AIChE Ethylene Producers Conference*, 218E.
125. Isberg, J., Hammersberg, J., Johansson, E., Wikström, T., Twitchen, D. J., Whitehead, A. J., Coe, S. E., . . . Scarsbrook, G. A. (2002). High carrier mobility in single-crystal plasma-deposited diamond. *Science*, 297, 5587, 1670–1672.
126. Dong, L., Tittel, F. K., Wright, J., Peters, B., Ferguson, B. A., & McWhorter, S. (2012). Compact QEPAS sensor for trace methane and ammonia detection in impure hydrogen. *Applied Physics B: Lasers and Optics*, 107, 2, 459–467.
127. Weast, R. C., & Astle, M. J. (1981). *61st CRC Handbook of Chemistry and Physics*. New York: CRC Press.
128. Bewley, W., Canedy, C., Kim, C. S., Kim, M., Lindle, J. R., Abell, J., . . . Meyer, J. (2010). Ridge-width dependence of mid-infrared interband cascade laser characteristics. *Optical Engineering*, 49, 11, 111116.
129. Lyakh, A., Maulini, R., Tsekoun, A. G., & Patel, C. K. N. (2010). Progress in high-performance quantum cascade lasers. *Optical Engineering*, 49, 111105.

130. Troccoli, M., Wang, X., & Fan, J. (2010). Quantum cascade lasers: High-power emission and single-mode operation in the long-wave infrared ($\lambda > 6 \mu\text{m}$). *Optical Engineering*, 49, 111106.

